Microbial hotspots in a relict fog-dependent Tillandsia landbeckii dune from the coastal Atacama Desert

Author(s):
Jaeschke, Andrea; May, S. Matthias; Hakobyan, Anna; Mörchen, Ramona; Bubenzer, Olaf; Bernasconi, Stefano M. (ID); Schefuß, Enno; Hoffmeister, Dirk; Latorre, Claudio; Gwozdz, Martina; Rethemeyer, Janet; Knief, Claudia

Microbial hotspots in a relict fog-dependent *Tillandsia landbeckii* dune from the coastal Atacama Desert

Andrea Jaeschke [a,*], S. Matthias May [b,*], Anna Hakobyan [c], Ramona Mörchen [d], Olaf Bubenzer [e], Stefano M. Bernasconi [f], Enno Schefuß [g], Dirk Hoffmeister [b], Claudio Latorre [h,i], Martina Gwozdz [j], Janet Rethemeyer [a], Claudia Knief [c]

[a] *Institute of Geology and Mineralogy, University of Cologne, 50674 Cologne, Germany*
[b] *Institute of Geography, University of Cologne, 50923 Cologne, Germany*
[c] *Institute of Crop Science and Resource Conservation, Molecular Biology of the Rhizosphere, University of Bonn, 53115 Bonn, Germany*
[d] *Institute of Crop Science and Resource Conservation, Soil Science and Soil Ecology, University of Bonn, 53115 Bonn, Germany*
[e] *Institute of Geography, Heidelberg University and Heidelberg Center for the Environment, Germany*
[f] *Geological Institute, ETH Zürich, Switzerland*
[g] *MARUM - Center for Marine Environmental Sciences, University of Bremen, Germany*
[h] *Centro UC Desierto de Atacama & Facultad de Ciencias Biológicas, Pontificia Universidad Católica de, Chile*
[i] *Institute of Ecology & Biodiversity (IEB), Santiago, Chile*
[j] *Institute for Nuclear Physics, University of Cologne, 50674 Cologne, Germany*

ARTICLE INFO

ABSTRACT

The hyperarid Atacama Desert in northern Chile is considered to be one of the most hostile habitats for microbial life. Despite the extreme environmental conditions, isolated patches of vegetation exist in an otherwise barren landscape. Unique dune ecosystems dominated by rootless *Tillandsia landbeckii* vegetation occur at elevations of about 900–1200 m asl within the coastal mountain range and receive water and nutrients mostly from the Pacific Ocean via fog deposition. The largest dunes can form over thousands of years, and may host diverse and abundant populations of microorganisms, sustained by fog moisture and nutrients via plant litter deposition. Relict dune ecosystems, with no living plants, are also common on this landscape. We investigated the microbial community structure in such a relict and stratified *Tillandsia* dune, located north of the Rio Loa canyon, to explore links between plant occurrence and past hydroclimatic variations using a multi-proxy approach. Our results indicated multiple phases of dune growth with alternating plant colonization, dieback, and sand accumulation during the past ~1300 years. Hydrogen isotope analysis of fossil leaf wax *n*-alkanes showed a distinct pattern of more humid conditions during the Medieval Climate Anomaly and increasing aridity during the Little Ice Age. We found that microbial abundance and diversity were generally higher in and just beneath core sections with elevated amounts of plant material. Recurrent rewetting events during specific climatic periods in the past may have supported active microbial communities in the sand dune, sustained by plant resources. This is further supported by significant changes in foliar and sedimentary $\delta^{15}N$ values. Most negative $\delta^{15}N$ values concurred with higher *n*-alkane abundances and distinct shifts in microbial community structure, pointing to increased biological nitrogen cycling in the central part of the dune, where niche occupation occurred by nitrifying *Thaumarchaeota*. In contrast, the upper part of the dune core was characterized by low microbial diversity and abundance. The community was dominated by members of the *Bacilli*, which may have dispersed via dust during a generally more arid climate. The sand dune thus retains a unique and well-preserved environmental record that reflects concomitant changes in past hydrological (i.e., fog) conditions, plant growth and microbial abundance and diversity during late Holocene climate extremes.

1. Introduction

The Atacama Desert in northern Chile is known to be one of the oldest and driest deserts on Earth (e.g., Dunai et al., 2005). The extreme aridity is caused by coupled subtropical atmospheric subsidence, coastal upwelling of cold northward flowing Humboldt current and the temperature inversion created through this interaction (Houston and Hartley, 2003). In addition, the rain shadow effect of the Andes is effectively blocking moisture transport from the Atlantic (Houston and Hartley, 2003; Houston, 2006; Garreaud et al., 2009). Due to its prevailing hyperaridity at least since the Miocene, intense UV-radiation and high salt and metal contents, the Atacama Desert is believed to be the most hostile habitat for microbial life and is often referred to as a Mars-analog environment (Navarro-González et al., 2003; Wierzchos et al., 2011; Azua-Bustos et al., 2012; Shen, 2020; Sager et al., 2023). Despite these extreme conditions, the threshold for life has not yet been reached and recent evidence has shown that soil systems are inhabited by a viable microbial community capable of switching between active and inactive states (Azua-Bustos et al., 2015; Schulze-Makuch et al., 2018; Rosinger et al., 2023). While precipitation is generally negligible (<2 mm/yr; Houston, 2006), fog water supply may be substantially higher across the coastal escarpment (Cereceda et al., 2008; Lobos Roco et al., 2018; Del Rio et al., 2021; García et al., 2021). Even low amounts of fog water may impact soil formation and soil organic carbon content (Mörchen et al., 2019, 2021; Voigt et al., 2020), while having a significant effect on ecosystem functioning and productivity in an otherwise barren landscape (Rundel et al., 1997; Pinto et al., 2006; García et al., 2021). Fog or cloud water can support microbial communities, which drive the majority of plant litter decomposition in water-limited regions (Jacobson et al., 2015; Dirks et al., 2017). In addition, fog can transport microbes from the ocean further inland, thereby increasing the diversity of microbial communities in desert ecosystems (Amato et al., 2005; Dueker et al., 2012; Evans et al., 2019).

In the coastal Atacama Desert, patches of highly diverse vegetation (called lomas) are maintained by advective coastal fog and occasional winter rainfall (Rundel and Dillon, 1998). In the main fog zone at elevations of about 900–1200 m above sea level (asl), vegetation is dominated by *Tillandsia landbeckii* (Pinto et al., 2006; Rundel et al., 1997; Koch et al., 2020). *T. landbeckii* is an epiphytic plant of the Bromeliaceae family and perfectly adapted to the extreme desert conditions by using highly specialized leaf trichomes for efficient water uptake (Raux et al., 2020) and crassulacean acid metabolism (CAM) for carbon assimilation (Haslam et al., 2003). The plants lack functional roots and occur as isolated stands or form continuous linear structures mostly on slopes oriented in southwest direction towards the incoming wind (Rundel et al., 1997; Borthagaray et al., 2010; Koch et al., 2020). *Tillandsia* dunes result from a succession of plant growth, dieback and new colonization, alternating with layers of wind-blown sand that accumulate over time. In cases where no living plants remain, the dunes become relicts of past *Tillandsia* distributions (Latorre et al., 2011). Based on radiocarbon dating, extensive *Tillandsia* dune fields may have persisted at least for the past ~3500 years (Latorre et al., 2011; Jaeschke et al., 2019). These studies also provided first evidence for paleoclimate variations during the late Holocene based on $\delta^{15}N$ analysis of relict plant material in distinct layers. The sedimentary archives of these dunes may retain a detailed record of past environmental change as shown for the Llamara Basin located north of the Rio Loa canyon at about 21°S (Finstad et al., 2018). Moreover, we expect them to host a characteristic microbiome, which is of importance for sustaining ecosystem function and highly sensitive to changes in environmental conditions, i.e., temperature, precipitation (Prieto et al., 2019; Hakobyan et al., 2023). Microbes can profit from carbon (C) and other resources released from plant litter, though their metabolic activity is strongly limited by the availability of water (Jones et al., 2018; Prieto et al., 2019; Alfaro et al., 2021). Two recent studies provide first evidence for the existence of specific bacterial communities associated with living *Tillandsia* plants (Alfaro et al.,

2021; Hakobyan et al., 2023). Distinct bacterial communities of higher diversity were found in the below-ground parts of the plants than aboveground (Hakobyan et al., 2023). Similarly, the soils below living *Tillandsia* plants hosted more diverse and larger populations compared to the sandy sites between viable *Tillandsia* rows (Alfaro et al., 2021). These differences in bacterial community structure were found to be related mainly to nitrogen (N) inputs, suggesting an uncommon and highly asymmetric plant-soil feedback in this extreme environment (Alfaro et al., 2021). However, vertical community profiles below *Tillandsia* plants remain unknown, but may contribute to the information content of these sedimentary archives.

In recent decades, the fog ecosystems of Chile have shown increasing signs of decline, but the underlying forcing mechanisms are not well understood (Schulz et al., 2011). Ongoing dieback of *Tillandsia* ecosystems from decreasing fog frequencies or changes in cloud cover (Muñoz et al., 2016; Del Rio et al., 2021; García et al., 2021) may also alter the structure of soil microbial communities, though possibly most strongly in surface-near layers. In this study, we investigated whether relict stratified *Tillandsia* dunes may also serve as specific habitat for diverse microorganisms as recently suggested (Alfaro et al., 2021; Hakobyan et al., 2023). To achieve this, we applied a combination of sedimentological, geochemical and microbiological techniques to a sediment sequence recovered from a relict *Tillandsia* dune located north of the Rio Loa canyon within the Coastal Cordillera of the Atacama Desert (Fig. 1). The microbial community composition in the dune was analyzed based on 16S rRNA gene amplicon sequencing and lipid biomarker analysis i. e., phospholipid fatty acids (PLFAs) and archaeal glycerol dialkyl glycerol tetraether lipids (GDGTs). The presence of living microorganisms was further assessed by a cultivation-based approach. Buried plant traits were identified by means of leaf wax *n*-alkane analysis (Knief et al., 2020; Mörchen et al., 2021; Contreras et al., 2022). Compound-specific hydrogen isotope analysis of these leaf wax *n*-alkanes was further used to characterize changes in hydrological conditions (Schefuß et al., 2005; Jaeschke et al., 2024). Variations in the depositional regime were depicted by grain size analysis and XRF-based elemental composition determination (Wennrich et al., 2023). In addition, buried plant material was radiocarbon-dated to develop a chronology of past dune growth (Latorre et al., 2011; Jaeschke et al., 2019). Our interdisciplinary approach therefore provides the first comprehensive view on the interplay between biotic and abiotic processes in relation with changes in environmental conditions during the past ~1300 years.

2. Materials and methods

2.1. Study area and sample collection

The study area is in the Coastal Cordillera of the Atacama Desert (Fig. 1), which separates the narrow coastal plain from the broad Central Valley (Houston and Hartley, 2003). We investigated a sand dune with buried *T. landbeckii* layers located about 27 km inland just north of the Rio Loa canyon (21°25′21.7" S, 69°48′13.76" W) at an elevation of 919 m asl (Fig. 1). The investigated dune is part of a field of relict *Tillandsia* dunes covering the southwest slopes of a ca. 75 m high bedrock ridge. Dead *T. landbeckii* plants are visible at the surface of the <1.50 m-high dunes between 915 and 950 m asl, partly covered by sand (Fig. 1d). At higher elevations (~1000–1150 m asl), about 2 km further northwest, patches of living *T. landbeckii* occur, mostly on southwest-facing slopes (Fig. 1c, populations 2 & 3 in Merklinger et al., 2020). Precipitation is extremely low (<2 mm/yr) but marine fog frequently enters through the Rio Loa canyon during most of the year (Schween et al., 2020; Böhm et al., 2021). Fog is thus an important source of water and nutrients for this *Tillandsia* ecosystem, as recorded for other populations (Pinto et al., 2006; González et al., 2011; Merklinger et al., 2020). Mean air (2 m above surface), soil surface and subsurface soil temperatures (10 cm below surface) recorded by meteorological stations in the study area between Feb 2018 and Feb 2023 are 16.2 °C, 20.5 °C and 22.8 °C at
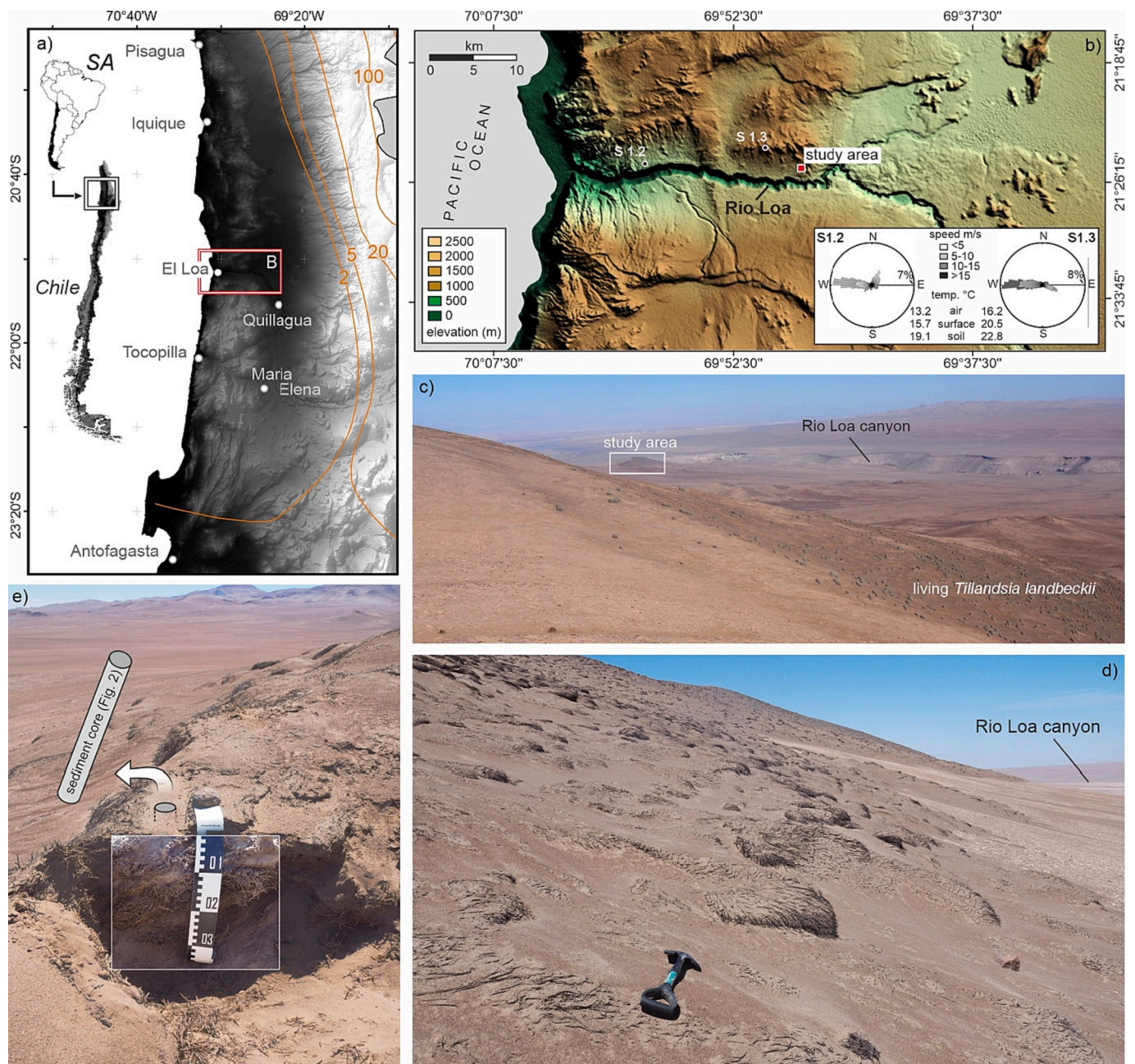
Fig. 1. (a) Map showing the location of the study area in the Atacama Desert, northern Chile. (b) Location of study area and weather stations S1.2 and S1.3 north of the Rio Loa canyon. Wind speed as well as air, surface and subsurface temperatures measured at S1.2 and S1.3 between 2018 and 2023 are shown in inlay. (c) View from S1.3 surround by living *Tillandsia* plants, towards the southeast, i.e., the study area (~2 km distance) and the Rio Loa canyon. (d) Lower slopes of the investigated field of relict *Tillandsia* dunes, with dead *Tillandsia* plants at the surface. (e) Close-up of the investigated relict *Tillandsia* dune with position of the push-core.

1150 m asl (weather station S1.3, 4.4 km to the northwest) and 13.2 °C, 15.7 °C and 19.1 °C at 700 m asl (weather station S1.2, 12.5 km to the west) (Fig. 1b; Hoffmeister, 2018a, 2018b). Wind is predominantly coming from the west with rare max. wind speeds of ~20 m/s at weather station S1.3 (Fig. 1b).

In September 2019, two consecutive push-cores (ca. 20 and 50 cm core length) were recovered from the centre of a relict dune in the lower part of the dune system using standard plastic tubes (7.5 cm diameter) from a local store (Fig. 1e). Tubes were sealed and shipped to Germany for further processing. The resulting core composite has a length of approximately 68 cm (Fig. 2). The cores were split in two halves, and the sampling strategy and resolution was defined based on visual inspection of the core, i.e., by distinct changes in lithology, colour and accumulated

plant residues (Fig. 2). One core half was used for sedimentological analyses (section 2.2) in order to characterize different sedimentary units found in the core. The other core half was used for radiocarbon dating (section 2.3) as well as geochemical and microbiological (sections 2.4–2.7) analyses on selected depth intervals of the core (see Supplementary Fig. 1 for a detailed sampling scheme).

2.2. Physical and chemical soil properties

The coarse- (>2 mm) and fine-grained (<2 mm) fractions from one core half ($n = 64$) were separated by sieving. About 1.5 g of the fine-grained fraction was then pre-treated by adding 15% H_2O_2 (to remove organic C), 10 ml of Na_2CO_3 (210 g/l; to dissolve gypsum contents), and
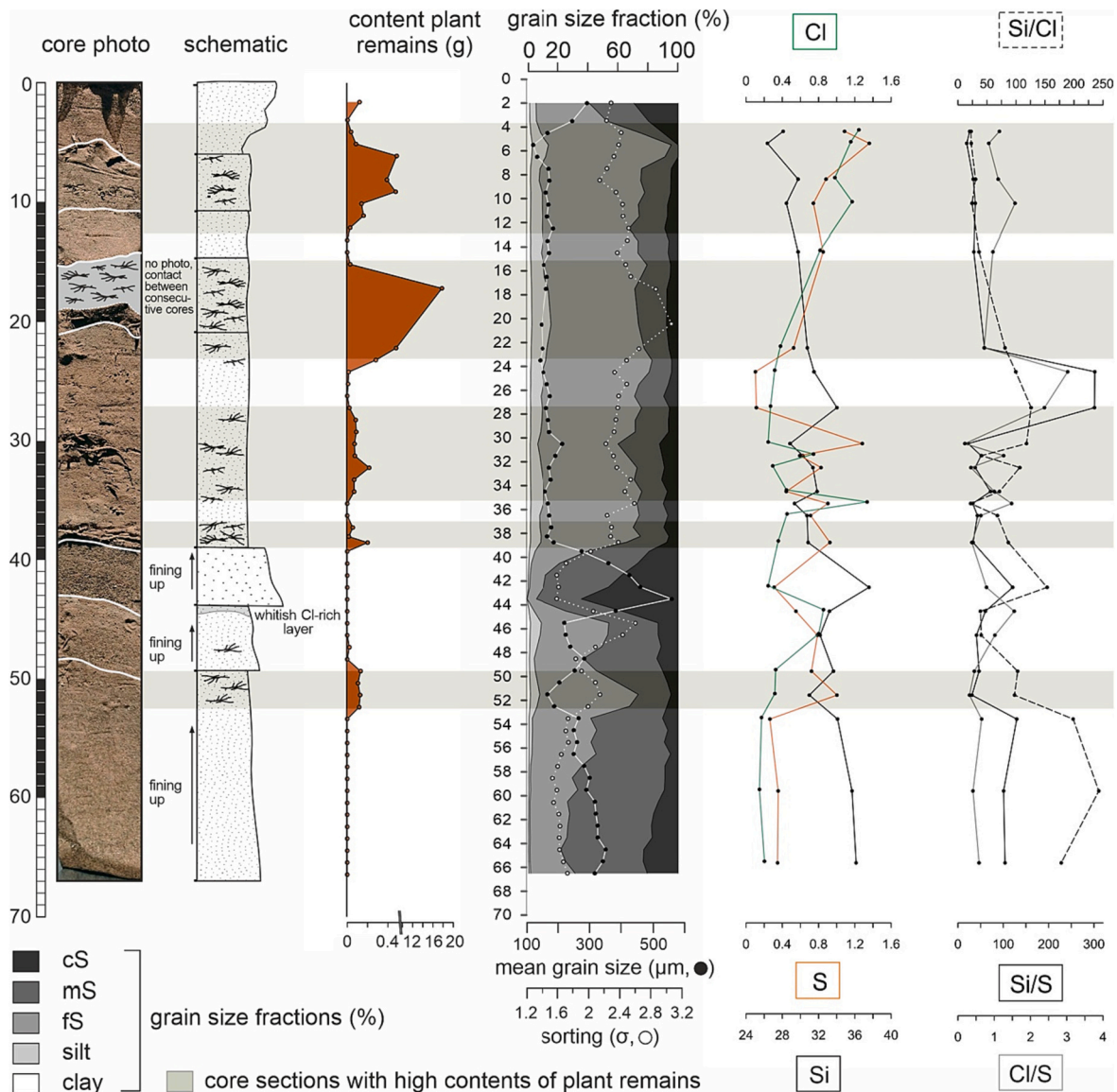
Fig. 2. Stratigraphy, grain size distribution and sorting, as well as elemental composition and ratios of the Rio Loa dune core.

15% HCl (to remove secondary carbonates) for granulometric analyses. The grain size distribution of each sample was measured using a Beckman Coulter LS 13320 Laser Particle Analyzer (Krefeld, Germany). Processing of univariate grain size statistical values and sorting was based on GRADISTAT software (Blott and Pye, 2001) and measures of Folk and Ward (1957). The inorganic element concentration of the untreated fine-grained fractions of selected samples ($n = 23$) was determined by means of non-destructive X-ray fluorescence (XRF) spectrometry. The bulk sample material (ca. 2 g) was homogenized, mixed with a wax binder (CEREOX Licowax at a ratio of 5 to 1), and pressed into 32 mm pellets. Measurements were then carried out using the Energy-Dispersive Polarisation XRF (EDPXRF) SPECTRO XEPOS P (SPECTRO Analytical Instruments Ltd. Kleve, Germany) analyzer under vacuum. Element concentrations are given in % of the total element content. For assessing variations in mineral composition and sediment source areas, visual interpretation of microscopic images was additionally performed on six selected samples using a Keyence VHX-2000 digital microscope with reflected light.

For elemental analysis, samples from 13 depth intervals of the second core half were further homogenized by milling (Retsch MM, Retsch, Hahn, Germany) at a frequency of 20 Hz for 2 min. Total carbon (TC),

total nitrogen (TN) and total sulfur (TS) contents were determined by weighing ca. 20 mg of sediment (referred to as S1-S13) and ca. 5 mg of plant material (referred to as P3-P13) into tin capsules and analyzed with an Vario MICRO cube elemental analyzer (EA, Elementar, Langenselbold, Germany). Analytical precision was 98% for C, 99% for N and 97% for S. The pH was measured with a glass electrode (Mettler Toledo) in soil slurries (1:2.5, w:w, soil/deionized water) in three-fold technical replication.

2.3. Radiocarbon analysis

Plant material collected from distinct depths of the second core half was used for radiocarbon dating (referred to as T1-T7, Supplementary Fig. 1). Plant tissue (ca 30–70 mg) was prepared by standard alkali-acid extraction followed by combustion and graphitization using a coupled system of an EA (Elementar, Germany) and an Automated Graphitization Equipment (AGE, Ionplus AG, Dietikon, Switzerland) according to the protocol of Rethemeyer et al. (2019). Radiocarbon analyses were performed at the Accelerator Mass Spectrometry (AMS) facility at the University of Cologne (CologneAMS), Germany. The age model is based on six AMS-^{14}C analyses performed on *T. landbeckii* plant material

Table 1

Radiocarbon ages obtained from buried *Tillandsia landbeckii* plant remains in a sand dune north of the Rio Loa.

Radiocarbon Lab ID[a]	Sample ID	Core depth (cm)	Fraction modern (F^{14}C)	^{14}C ages ±1σ error (yr BP)	2σ calibrated ^{14}C age range (cal yr BP)[b]	Median probability (cal yr BP)
COL7112.1.1	T1	10	0.964 ± 0.004	292 ± 36	460–158	308
COL6991.1.1	T2	17.5	0.973 ± 0.004	219 ± 33	420-modern	193
COL6992.1.1	T4	30	0.902 ± 0.004	830 ± 34	787–680	705
COL7114.1.1	T5	37.5	0.881 ± 0.004	1017 ± 40	1051–793	861
COL7115.1.1	T6	47.5	0.859 ± 0.004	1226 ± 39	1275–1060	1096
COL6993.1.1	T7	52.5	0.858 ± 0.004	1231 ± 34	1271–1065	1103

[a] COL (Cologne AMS, University of Cologne, Germany).

[b] Radiocarbon ages were calibrated with Calib 8.2 (Stuiver et al., 2020) and the SHCAL20 Southern Hemisphere calibration dataset (Hogg et al., 2020).

(Table 1). All AMS ^{14}C-ages were converted to calendar ages (cal yr BP; present is 1950 AD) using the CALIB 8.2 software (Stuiver et al., 2020) with the SHCal20 Southern Hemisphere calibration curve (Hogg et al., 2020). The age model was constructed using the Bayesian program BACON implemented in R (Blaauw and Christen, 2011).

2.4. Carbon, nitrogen and sulfur stable isotope analysis

Carbon (δ^{13}C) and nitrogen (δ^{15}N) isotopes were analyzed in aliquots of the homogenized bulk sediment (S1-S13) and plant fractions (P3-P13) from the 13 depth intervals (Supplementary Fig. 1) on a Thermo Fischer Scientific Flash Elemental Analyzer (EA) (1112 Series) interfaced with a Conflo III to a Delta V Advantage Isotope Ratio Mass Spectrometer (IRMS). Isotope ratios were calculated and normalized using a number of reference standards: acetanilide (A. Schimmelmann) δ^{13}C = −27.53‰ and δ^{15}N = +1.18‰), ammonium sulfate (IAEA-N2) δ^{15}N = +20.3‰), cellulose (IAEA-CH3) δ^{13}C = −24.72‰ and corn starch (A. Schimmelmann) δ^{13}C = −11.01‰. Analytical precision was 82% for δ^{13}C and 76% for δ^{15}N. Bulk sediment sulfur (δ^{34}S) isotopes were analyzed on a ThermoFisher Flash-EA 1112 elemental analyzer coupled via a Conflo IV interface to a ThermoFisher Delta V isotope ratio mass spectrometer. The system was calibrated with the reference materials NBS 127 (δ^{34}S = 21.1‰), IAEA-SO-5 (δ^{34}S = +0.49‰), and IAEA-SO-6 (δ^{34}S = −34.05‰) for sulfates.

All analytical results are reported in δ notation, in per mil relative to the Vienna Pee Dee Belemnite (VPDB) for C, to atmospheric nitrogen (AIR) for N, and to the Vienna Canon Diablo troilite (VCDT) for S. Reproducibility based on duplicate measurement of samples was 0.18‰ for TC, 0.23‰ for TN, and 0.38‰ for TS.

2.5. 16S rRNA gene analysis

2.5.1. DNA extraction and 16S rRNA gene quantitative PCR

Aliquots of the homogenized sediment samples from 13 depth intervals (S1-S13, Supplementary Fig. 1) were used for DNA extraction conducted with the NucleoMag DNA Microbiome kit (Macherey-Nagel) with few modifications (see Supplementary information). DNA concentration in all extracts and the extraction control was quantified using the QuantiFluor®dsDNA System (Promega Corporation, Fitchburg, WI) and DNA stored at −20 °C for further use.

Quantitative polymerase chain reaction (qPCR) was applied to quantify archaeal and bacterial 16S rRNA gene copy numbers in the samples. Primer combination Bac349f/Bac806r (Takai and Horikoshi, 2000) was used for bacterial and Arch349f/Arch806r (Wei et al., 2019) for archaeal genes. The qPCR was conducted in 96-well microtiter plates (BioRad) using SsoAdvanced Universal SYBR Green Supermix (BioRad) on a CFX Connect™ Real-Time PCR Detection System (BioRad), as described by Frindte et al. (2020) with some modifications (see Supplementary information). All reactions were carried out in three technical replicates. The PCR efficiency was between 85% and 115% (R^2 > 0.97). Data were normalized to gene copy numbers per g dry sediment.

2.5.2. Bacterial and archaeal 16S rRNA gene PCR and amplicon sequencing

The extracted DNA was used for 16S rRNA gene targeted PCR to prepare products for amplicon sequencing. The amplification was done in triplicates per sample in a two-round-PCR approach. In both rounds the DNA was amplified using primer set 515f/806r (Caporaso et al., 2011). The first round consisted of a 25-μl PCR reaction mixture with 5 μl of 5× polymerase buffer, 0.25 μl of each primer [25 mM], 0.25 μl of dNTP mixture [25 mM each dNTP], 1 μl of MgCl$_2$ [50 mM], 0.25 μl of Herculase II Fusion DNA polymerase [5 U/L] (Agilent Technologies), 3 μl of DNA template and PCR-grade water (Qiagen). The PCR reaction was conducted in 30 cycles (95 °C, 30 s; 52 °C, 30 s for 515f/806r primer annealing; 72 °C, 45 s) upon initial denaturation at 95 °C for 4 min. PCR was finalized by elongation at 72 °C for 10 min. The triplicate PCR products were pooled before the second round. For the second PCR primers 515f/806r were used with sample-specific 8mer barcodes as published (Frindte et al., 2019). It was performed in 3 × 50 μl assays with 5 μl of template from the first round by applying a temperature profile consisting of initial denaturation, 8 cycles and final elongation as before. The three replicates of each sample were pooled and DNA concentration quantified using the QuantiFluor dsDNA system (Promega). For the amplification of archaeal 16S rRNA genes the bacterial primer pair was replaced in the above described first-round PCR mixture by the archaeal primers 20f/958r (Ochsenreiter et al., 2003). The PCR was performed with 35 cycles (54 °C, 20 s for primer annealing). The second PCR round was performed as described above, but with the barcoded primer 515f in combination with Arch806r and by applying 35 cycles. PCR products of the different samples were pooled at equimolar ratios and the resulting pool was purified and concentrated using the High-Prep™PCR Clean-up System kit (MagBio Genomics, Gaithersburg, MD). Upon running the pooled PCR products on an agarose gel, bands of the correct size were excised and purified from agarose gel using the QIAEX II gel extraction kit (Qiagen). Library preparation and sequencing were done by the West German Genome Center (WGGC) on a MiSeq platform (Illumina) generating 2 × 300 bp paired end reads.

2.5.3. Sequence data analysis and visualization

The raw sequence reads were processed as described before (Hakobyan et al., 2023). In brief, the samples were demultiplexed, primers removed and further processed with QIIME2 version 2022.2 (Bolyen et al., 2019) including denoising using default parameters of DADA2 (Callahan et al., 2016) implemented in QIIME2. Quality-filtered reads were grouped into amplicon sequence variants (ASVs). The taxonomic assignment of ASVs was done against the SILVA SSU138 Ref NR99 database (Quast et al., 2013; Yilmaz et al., 2014). Unassigned ASVs as well as ASVs classified as mitochondria, chloroplasts and *Eukaryota* were removed. Rare ASVs that appeared with <20 reads across all samples or in less than five samples were also removed. Samples with <5000 reads remaining were excluded from further analyses (S13 and DNA extraction control). The dataset was then exported and was further analyzed using the phyloseq R package (version 1.44.0) (McMurdie and Holmes, 2013).

Diversity analyses were performed in the QIIME2 environment and

in R version 4.2.0 (http://www.r-project.org/index.html). Alpha diversity was estimated by Shannon's diversity index and Chao1 richness index using the estimate_richness function of the phyloseq R package based on the feature table rarefied to 5000 reads per sample. No statistical tests were applied, since each sample type was unique within each category. Differences in the bacterial community composition were summarized in a Bray-Curtis distance matrix upon Hellinger transformation. Sample dissimilarities and their correlations to sediment physicochemical parameters were visualized by distance-based redundancy analysis (dbRDA) using the capscale function of the vegan package (Oksanen et al., 2022) for constrained canonical analysis of principal coordinates. Statistical differences were calculated for the measured soil physicochemical parameters using a permutation test for constrained correspondence analysis (*anova.cca*) on the dbRDA model (*vegan* package). The visualization of the data was done in R using ggplot2 (Villanueva and Chen, 2019).

2.5.4. Estimation of viable cell counts

The number of culturable bacterial cells in the sediment layers S1-S13 (Supplementary Fig. 1) was estimated by the viable plate method. One gram of each sediment sample was diluted in 10 ml of $1\times$ phosphate buffered saline (PBS) and vortexed vigorously to separate the bacteria from the soil particles. The 500 µl of undiluted (10^0) sample was transferred to a 2-ml sterile microcentrifuge tube and used for a 1:10 dilution series ($10^{-1}, 10^{-2}, 10^{-3}$). Reasoner's 2 A (R2A, VWR International) was used as medium to monitor the growth of bacterial cells on agar plates. Plates were incubated at 30 °C and evaluated for bacterial growth over a period of 72 h. Counts were used to calculate the number of colony forming units per gram of sediment dry weight (CFU/gDW sediment). The obtained cell counts served as proxy for the presence and abundance of viable cells, enabling a comparison between the different sediment layers (S1-S13) of the *Tillandsia* dune.

2.6. Lipid biomarker analysis

2.6.1. Lipid extraction and fractionation

Aliquots (ca. 32–66 g) of the homogenized sediment samples from 13 depth intervals (S1-S13, Supplementary Fig. 1) were extracted in 1 L Schott flasks following the modified Bligh and Dyer protocol of Wilhelm et al. (2017). A detailed description can be found in Rosinger et al. (2023). Briefly, Milli-Q water, methanol (MeOH) and dichloromethane (DCM) were used for the extraction, followed by base hydrolysis to liberate ester-bond fatty acids. The total fatty acid pool (PLFAs and free fatty acids) was repeatedly extracted with DCM from the aqueous solution at pH 1 and transesterified with MeOH:HCL$_{conc}$ (95:5; v:v) to form fatty acid methyl esters (FAMEs). FAMEs were further purified over a small silica gel column and elution with DCM:*n*-hexane (2:1, v:v). The polar rest containing GDGTs was eluted with MeOH. Non-saponifiable (neutral) lipids released from the basic solution were further separated by silica gel column chromatography and *n*-hexane and DCM/MeOH (1:1, v:v) to elute *n*-alkanes and GDGTs, respectively. The apolar fractions containing *n*-alkanes were further separated into saturated and unsaturated compounds using small columns filled with AgNO$_3$ coated silica gel (10% *w*/*w*) and *n*-hexane and DCM, respectively. GDGTs present in the neutral and fatty acid fractions were combined, dissolved in *n*-hexane:isopropanol (95:5, v:v) and filtered through 0.45 µm polytetrafluoroethylene (PTFE) filters prior to analysis.

2.6.2. GC analysis

FAMEs were identified using an Agilent 6890 N gas chromatograph (GC) coupled to an Agilent 5975C MSD (Santa Clara, California) and by comparison with an external Bacterial Acid Methyl Ester Mix (BAME; Supelco) as described in Rosinger et al. (2023). *n*-Alkanes were analyzed using a gas chromatograph equipped with an on-column injector and a flame ionization detector (GC-FID; Agilent 7890 series II; Santa Clara, California). A fused silica capillary column (Agilent DB-5MS; 50 m × 0.2

mm, film thickness: 0.33 µm) was used with He as carrier gas. The compounds were quantified against authentic external FAME and *n*-alkane standard mixtures (Supelco). Analytical precision of the quantifications based on replicate standard analyses was >95%. Standard nomenclature was used to describe the PLFAs.

2.6.3. HPLC-MS analysis

GDGTs were analyzed using ultra-high performance liquid chromatography (UHPLC; Agilent 1290 Infinity, Santa Clara, California) coupled to an Agilent 6460 Triple Quad - atmospheric pressure chemical ionization-mass spectrometer (QQQ-APCI-MS, Santa Clara, California) according to Hopmans et al. (2016). To improve separation, two UHPLC silica columns (BEH HILIC columns, 2.1, 150 mm, 1.7 µm; Waters, Milford, MA) were coupled in series and fitted with a 2.1 cm long, 5 mm diameter pre-column of the same material. Individual GDGTs were detected via single ion monitoring (SIM) using *m/z* 744 for the internal standard, *m/z* 1302, 1300, 1298, 1296, and 1292 for isoprenoid (iso) GDGTs including crenarchaeol and its isomer. Concentrations of GDGTs were quantified using an internal C$_{46}$ standard (Huguet et al., 2006) and assuming a similar mass spectrometric response for all compounds.

2.7. Compound-specific hydrogen isotope (δD) analysis

The hydrogen isotope (δD) analyses of the most abundant *n*-alkane homologues (*n*-C$_{23}$-*n*-C$_{31}$) detected in the sediment (S1-S12) and plant (P6-P7) fractions were performed on a Thermo Trace GC (Waltham, MA) coupled to a Thermofisher MAT 253 isotope ratio mass spectrometer (Bremen, Germany) via a GC IsoLink with a pyrolysis reactor operated at 1420 °C, respectively. The GC was equipped with 30 m × 0.25 mm column (Restek Rxi-5 ms, film thickness: 1.0 µm) and He was used as the carrier gas. The method used in this study followed the one described in Jaeschke et al. (2024). Each sample was analyzed in duplicate if sufficient material was available. Isotope values were calibrated against H$_2$ reference gas and are reported in ‰ relative to Vienna Standard Mean Ocean Water (VSMOW). The long-term precision monitored by external standard analyses was <3‰ for δD.

3. Results

3.1. Sedimentological properties of the dune

The entire sedimentary succession recorded by the push-core was sand-dominated, although *T. landbeckii*-bearing layers were indicated by a typical and consistent grain size distribution compared to *T. landbeckii*-free layers (Fig. 2). At its base, the core started with a layer of moderately well sorted medium sand (mean ~ 330 µm), which fined upwards to poorly sorted fine sand (~170 µm) with slightly higher silt and clay contents (>5%). Here, the lowermost *T. landbeckii* remains of the core were found at ca. 50–53 cm depth below surface (b.s.). Above, an abrupt boundary followed a *T. landbeckii*-free layer of medium (bottom) to slightly silty fine (top) sand. In the uppermost cm of this layer chlorine (Cl) contents increased, related to a one-cm-thick whitish lamina (Fig. 2). After a further abrupt, possibly erosive boundary, moderately well sorted coarse sand (~560 µm) occurred, which was again fined upwards to poorly sorted fine sand (~166 µm) at 39–44 cm b.s. The coarse sand found at the base of that layer resembled the material building large wind ripples that are found on the surface in the surroundings of the studied *Tillandsia* field (Supplementary Fig. 2). Above, (ca. 20–39 cm b.s.) a unit of poorly sorted fine sand (~160 µm) with higher silt (5–10%) and clay (~2–3%) contents with abundant *T. landbeckii* remains occurred, only interrupted by a thin sand layer free of plant remains (~24–27 cm b.s.). Here, reduced S contents were inferred based on the XRF results (Fig. 2). Subsequently, a thick *T. landbeckii* layer (~15–20 cm b.s.) followed, which was covered by further *T. landbeckii*-free units and one more *T. landbeckii*-containing (~6–11 cm b.s.) layer. Finally, in the upper part of the core (~0–6 cm b.

s.), poorly sorted fine to medium sand not containing any plant remains built the top of the dune.

Microscopic analyses (Supplementary Fig. 3) revealed that most sand grains from all samples were moderately well rounded and showed dim/matt surfaces with impact marks, typical for sand transported by aeolian processes. In addition, all samples showed a similar spectrum of predominantly igneous rocks and minerals (quartz, amphibole, pyroxene, epidote), documenting a uniform mineralogical content for all investigated samples. However, in most samples angular and mostly non-matted grains were found as well, pointing to deflation of sediment sources other than those stemming from the aeolian process system, i.e., past and present dune sand or sand ripples, as occurring on the shoulders of the Rio Loa canyon and in direct adjacency of the study site (Supplementary Fig. 2). In the samples taken from and below the whitish lamina with elevated Cl contents (~44–47 cm b.s.), gypsum/anhydrite crystals frequently occurred in the silt fraction. Grains from these samples appeared "dirty" due to whitish coatings, likely related to mobilization and secondary precipitation of soluble salts.

3.2. Chronostratigraphy

The dune profile contained discrete layers of *T. landbeckii* remains of varying thickness (T1-T7) and ^{14}C data revealed a clear trend of increasing age with depth from the dune crest (Table 1; Supplementary Fig. 4). The upper ca. 20 cm of the core were characterized by abundant plant material (Fig. 2), likely representing interwoven plant layers of a similar age (T1-T2; Table 1). ^{14}C ages in this upper part of the core were comparable to those of other relict dune surfaces (Jaeschke et al., 2019) suggesting similar environmental conditions that caused dieback at around 310 cal yr BP (Table 1). Layers T6 and T7 were more or less interwoven and also revealed similar ages. The ^{14}C age of the basal layer indicated that dune growth started at approximately 1230 cal yr BP. Accumulation rates based on ^{14}C ages and age-depth modelling (Bacon) averaged to 0.047 cm/yr ($\pm$0.01 cm/yr) and varied between 0.031 cm/yr to 0.063 cm/yr (Supplementary Fig. 5). Lowest but relatively constant rates were observed between ca. 20–30 cm depth, while higher accumulation occurred below ca. 30 cm and in the upper part of the core from ca. 20 cm, likely related to the higher amount of plant material (Fig. 2) acting as sand trap during the past ~400 years.

3.3. Chemical characterization and stable isotope analysis

The sediment fractions (S1-S13) were characterized by slightly alkaline pH values ranging between 7.4 and 7.9 (Table 2). In general, low TC of 0.04–0.26% (mean 0.16%) and TN contents of 0.02–0.04% (mean 0.03%) were observed throughout the core (Table 2). C/N ratios ranged between 2 and 9. The TS content varied between 0.2 and 0.5% (mean 0.34%). Surface layers showed very low values in most cases, but otherwise there was no consistent change with increasing depth.

Compared to the sediment fraction, the plant fractions (P3-P13) were characterized by higher TC and TN contents of 0.1–15.4% (mean 6.8%) and 0.06–0.39% (mean 0.23%), respectively (Supplementary Table 1). C/N ratios ranged between 2 and 40 (mean 25), reflecting the variable amount of plant material in the core. TS was also higher in plant than in the sediment layers and ranged between 0.1 and 2.7% (mean 1.1%).

Sedimentary δ^{13}C values ranged between −12.1‰ and − 8.1‰ (Table 2), whereas the plant material revealed more ^{13}C-depleted values that varied between −14.9‰ and − 11.0‰ (Supplementary Table 1). Sedimentary δ^{15}N values ranged between −0.2‰ and + 5.5‰ (Table 2), whereas plant δ^{15}N values were in general more negative and varied between −6.4‰ and + 3.7‰ (Supplementary Table 1). The most depleted ^{15}N values in the sediment samples (S4-S9) were related to intervals with high amount of plant fragments (S4-S9). Otherwise, there was no consistent change in δ^{13}C and δ^{15}N with increasing depth. Sedimentary δ^{34}S values exhibited only minor variation between +10.7‰ and + 11.7‰ (mean + 11.0 ‰) in the core (Table 2).

3.4. Total and viable microbiota of the Tillandsia dune

We used cultivation-dependent and independent methods to estimate the microbial biomass present in the sediment layers S1-S13 (Supplementary Fig. 1). Colony counting of cultivable cells revealed the presence of viable bacterial cells at all depth intervals of the core, ranging from 10^3 to 10^6 CFUs/g sediment (Fig. 3a). We noticed a clear increase in the CFU counts in layers S2 to S4, with subsequent decrease with increasing depth of the core. In layers S9 to S13, CFU counts stayed at a relatively similar level around 3.2×10^3 CFUs/g sediment.

To analyze the bacterial and archaeal abundance in the sediment, qPCR of the 16S rRNA genes was performed. We detected both, archaeal and bacterial 16S rRNA gene copies in all 13 layers (Fig. 3b). Though, bacterial abundance (1.5×10^4 to 3.5×10^6 gene copies/g dry sediment) was an order of magnitude higher than archaeal abundance (4.6×10^3 to 2.2×10^5 gene copies/g dry sediment). Interestingly, both of the groups demonstrated sharp increase in 16S rRNA gene copy numbers in the middle layers of the core (S5-S7) (Fig. 3b; Supplementary Table 2). Moreover, there was a slight increase in bacterial abundance towards the deepest layers (S12 and S13) of the core.

16S rRNA gene amplicon sequencing revealed that the bacterial community was dominated by different classes of *Bacilli* in the upper and lower parts of the core with minor contributions of *Bacteroidia*, *Gamma*- and *Alphaproteobacteria* as well as *Deinococci* (Fig. 4a). In contrast, the middle core section hosted a much higher diversity of bacteria dominated by *Bacteroidia*. *Actinobacteria* were mostly present in layers S8-S9 and absent in the upper part of the core (S1-S4). The archaeal community composition, targeted using specific primers, could only be assessed in four depth layers (S6, S7, S12, S13) due to extremely low numbers of target genes in the extracts. The most dominant domain was *Thaumarchaeota* Group 1.1b, while a contribution of *Euryarchaeota* was minor
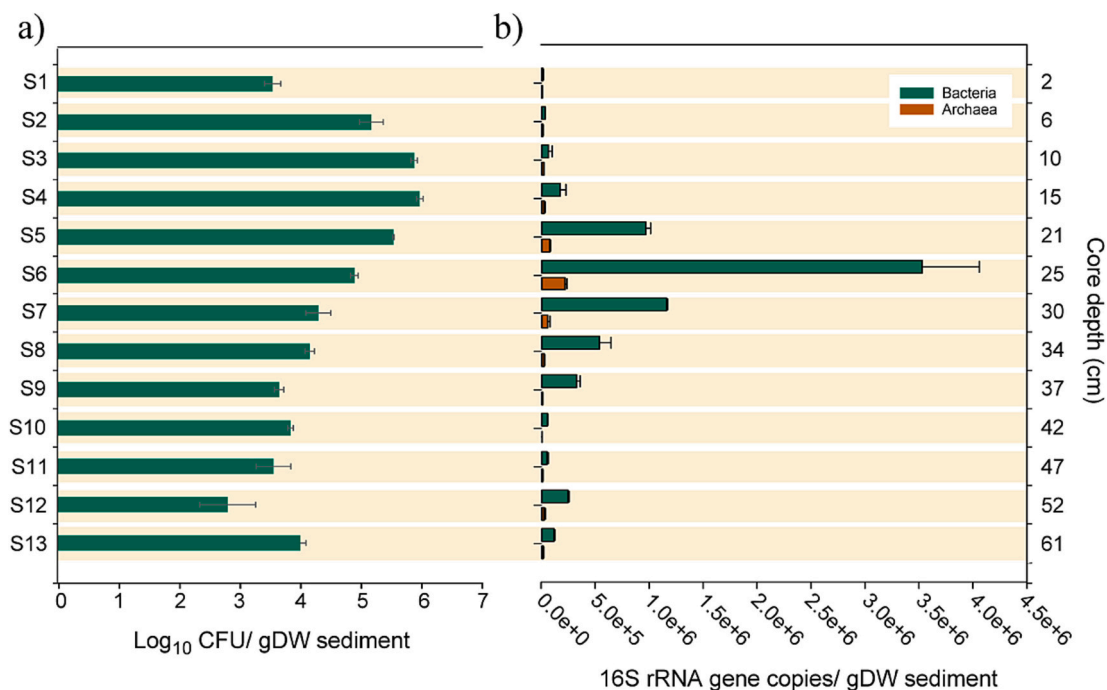
Table 2
Radiocarbon ages, pH, elemental composition and stable carbon, nitrogen and sulfur isotopic composition of bulk sediment (F < 1 mm) analyzed in distinct depth intervals (S1-S13) of the Rio Loa core.

Sample ID	Depth (cm)	Age (yr cal BP)	pH	C (%)	N (%)	S (%)	C/N	δ^{13}C (‰)	δ^{15}N (‰)	δ^{34}S (‰)
S1	2	40	7.40	0.07	0.03	0.32	2.4	−10.2 ± 0.8	4.8 ± 0.4	10.7 ± 0.1
S2	6	119	7.56	0.10	0.04	0.51	2.8	−8.1 ± 0.2	5.5 ± 0.1	11.0 ± 0.3
S3	10	198	7.58	0.15	0.03	0.38	4.8	−8.3 ± 0.0	4.5 ± 0.3	10.9 ± 0.1
S4	15	294	7.53	0.26	0.03	0.36	9.2	−9.4 ± 0.2	2.0 ± 0.0	11.3 ± 0.3
S5	21	464	7.36	0.24	0.04	0.37	6.6	−10.6 ± 0.3	1.9 ± 0.1	11.0 ± 0.1
S6	25	556	7.63	0.24	0.04	0.26	6.5	−11.2 ± 0.1	−0.2 ± 0.0	11.0 ± 0.9
S7	30	695	7.72	0.19	0.03	0.47	5.6	−11.0 ± 0.1	0.5 ± 0.4	11.7 ± 0.1
S8	34	789	7.65	0.23	0.03	0.25	7.7	−9.9 ± 0.1	0.6 ± 0.3	11.1 ± 0.6
S9	37	846	7.89	0.15	0.03	0.36	5.4	−10.0 ± 0.1	2.2 ± 0.6	11.7 ± 0.0
S10	42	947	7.84	0.04	0.02	0.24	2.4	−12.1 ± 0.3	3.5 ± 1.3	11.4 ± 0.1
S11	47	1049	7.41	0.18	0.03	0.39	5.4	−8.9 ± 0.2	3.5 ± 0.2	11.0 ± 0.7
S12	52	1124	7.63	0.14	0.03	0.36	5.0	−9.6 ± 0.1	3.6 ± 0.1	11.1 ± 0.6
S13	61	1329	7.77	0.04	0.02	0.20	2.0	−10.7 ± 0.1	3.6 ± 0.8	10.9 ± 1.0

Fig. 3. (a) Bacterial colony forming units (CFUs) in sediments from distinct depth intervals (S1-S13) of the Rio Loa core. Mean values and standard deviation of two experimental replicates are shown. (b) 16S rRNA gene copy numbers indicate changes in bacterial and archaeal abundance along the same depth profile. Shown are mean values with standard deviation of three technical replicates.

(Supplementary Fig. 6). In layers S6 and S7, the order *Nitrosphaerales* was predominant, represented by '*Candidatus* Nitrocosmicus'. Layer S12 revealed in addition members of the *Halobacterales* (genus *Halomicrobium*), whereas members of the *Thermoplasmata* were exclusively detected in S13.

Bacterial alpha diversity based on Shannon's index calculated from the amplicon sequencing data showed a similar pattern over depth as seen for the 16S rRNA gene abundance (Fig. 4b). The bacterial diversity and also the estimated species richness (Chao1) increased in the central part of the core (layers S5-S7). Nonetheless, the central peak in the Chao1 index was not as clear as for Shannon's diversity, underlining that lower evenness, evident from the unequal distribution of relative abundances (Fig. 4b), contributed to the increase in Shannon's index in the central part of the core. Both the diversity and the richness increased slightly in the deepest layer of the core (S12).

The constrained ordination analysis showed a clear clustering of the samples into distinct layer groups and the presented two dimensions of the plot reflected 62% of the constrained variation seen in the bacterial amplicon data (Fig. 4c). The clustering could be well related to measured physicochemical parameters of the sediments and was significantly distant especially along the first axis (F = 7.76, $p = 0.05$). The bacterial community in the upper four layers of the core was positively related to $\delta^{13}C$, and S and negatively to $\delta^{34}S$. The bacterial community composition in the central part of the dune core (layers S5-S7) clustered very distinct from the other samples and this was positively driven by C, N, and C/N, while isotopic signatures of C and N were negatively related. Next, pH was an important factor being positively related in particular the bacterial community composition in the deeper layers (S9 to S11).

3.5. Bacterial and archaeal lipid biomarkers

Total PLFA concentrations in the sediment layers S1-S13 ranged between 69 and 1877 ng/g sediment (Supplementary Table 3; Fig. 5a). Highest abundances were observed in the upper-middle section of the core (S4-S7), where also most plant fragments were found. The PLFA pool was further separated based on structural differences characteristic for distinct bacterial groups (e.g., Kaur et al., 2005; Willers et al., 2015). PLFAs were generally dominated by saturated fatty acids (Sat) in the range C_{12}-C_{20} with 44–82%, followed by $C_{16:1}$ and $C_{18:1}$ monoenoic fatty acids (MUFA, 7–44%), $C_{15:0}$ and $C_{17:0}$ terminally branched saturated fatty acids (TerBrSat, 4–40%), the mid-branched saturated fatty acid 10-Me $C_{16:0}$ (MidBrSat, 0.5–8%), the polyenoic fatty acid $C_{18:2(\omega9,12)}$ (PUFA, 0.3–7%) as well as low abundances of $C_{17:0}$ and $C_{19:0}$ cyclopropyl fatty acids (Cyclo, <1.5%) (Supplementary Table 3; Fig. 5a).

Iso-GDGTs, specific membrane lipids of archaea (see review by Schouten et al., 2013), were also detected in all samples. GDGTs were much lower in abundance compared to PLFAs and ranged from 19 pg/g to 10.2 ng/g sediment (Supplementary Table 4; Fig. 5b). The extremely low abundance and distribution of archaeal traits in the sediments confirmed our 16S rRNA gene-based results (Fig. 3b). The abrupt increase in GDGT abundance at about 25 cm depth (S6) was slightly offset to that of PLFAs (S5), but is in line with the maximum in archaeal 16S rRNA genes (Fig. 3b; Supplementary Table 2). GDGTs were dominated by GDGT-0 and Crenarchaeol, while additional GDGTs with 1–4 ring moieties as well as the Crenarchaeol isomer (Cren') indicative of *Thaumarchaeota* (Schouten et al., 2013), were only detected in layers S6 and S7 (Fig. 5b), in agreement with the archaeal community composition (Supplementary Fig. 6). GDGT-based temperature estimates were 22.6 °C (S6) and 22.5 °C (S7), respectively (Supplementary Table 4), which is surprisingly similar to measured soil temperature from the nearby weather station (Supplementary information 1).

3.6. Distribution and isotopic composition of leaf wax n-alkanes

Long-chain *n*-alkanes indicative of higher plant material, were identified in all sediment samples (S1-S13) with concentrations of 7–560 ng/g (Supplementary Table 5), while concentrations in the plant fractions (P6-P7) were about 10–100 times higher (Table 3). Highest *n*-alkane concentrations were observed in the upper-middle sections of the core, consistent with the generally higher occurrence of plant fragments (Fig. 2). Leaf wax *n*-alkanes showed an almost homogeneous chain
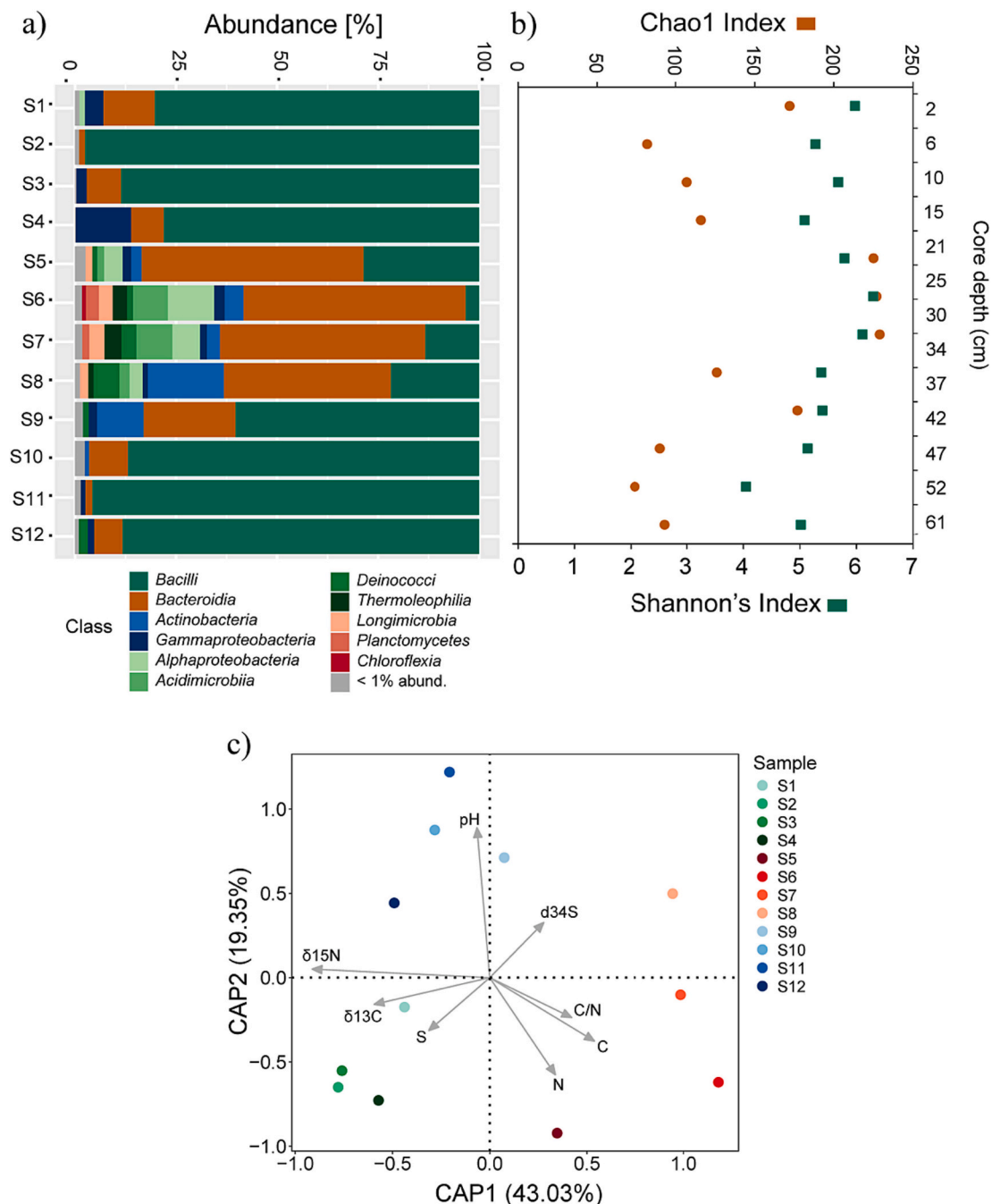
Fig. 4. (a) Bacterial community composition in sediments from distinct depth intervals (S1-S12) of the Rio Loa core. Shown are relative abundances of the different classes with >1% relative abundance. (b) Chao1 index and Shannon's index indicate changes in bacterial alpha diversity. (c) Bray-Curtis distance-based redundancy analysis (db-RDA) shows the influence of sediment physicochemical properties on the samples according to their similarities in the upper, middle and lower core sections.

length distribution between n-C_{23} and n-C_{31} (Supplementary Fig. 7). Likewise, average chain length (ACL) values showed a relatively narrow range of 26.9 to 27.9 (mean ACL 27.4) in both fossil plant fragments and sediments. Carbon preference index (CPI) values of the plant fractions were on average 6.5, while sedimentary CPI values were lower and ranged between 2.0 and 3.8 (Table 3; Supplementary information 1).

Compound-specific δD values of the most abundant leaf wax n-alkanes (C_{23}-C_{31}) in the sediments varied between −170‰ and 141‰ (Table 3). Only two depth intervals of the core (P6-P7) had enough plant material for δD analysis. Plant δD values varied between −166‰ and −147‰, thus were in a similar range compared to the respective sediment fractions. Because of the almost even distribution of the different n-

alkane homologues, we calculated the weighted average isotopic composition (δD$_{wax}$) as proposed by Jaeschke et al. (2024). Sedimentary δD$_{wax}$ values varied between −166‰ and 151‰. In addition, plant δD$_{wax}$ values were identical to those from the sediment of the same depth intervals (Table 3; Fig. 6e).

4. Discussion

4.1. A paleoclimate record for past variations in fog amount

In desert regions, paleo-environmental studies are scarce, mainly due to the lack of suitable archives (e.g., lake records). Absolute
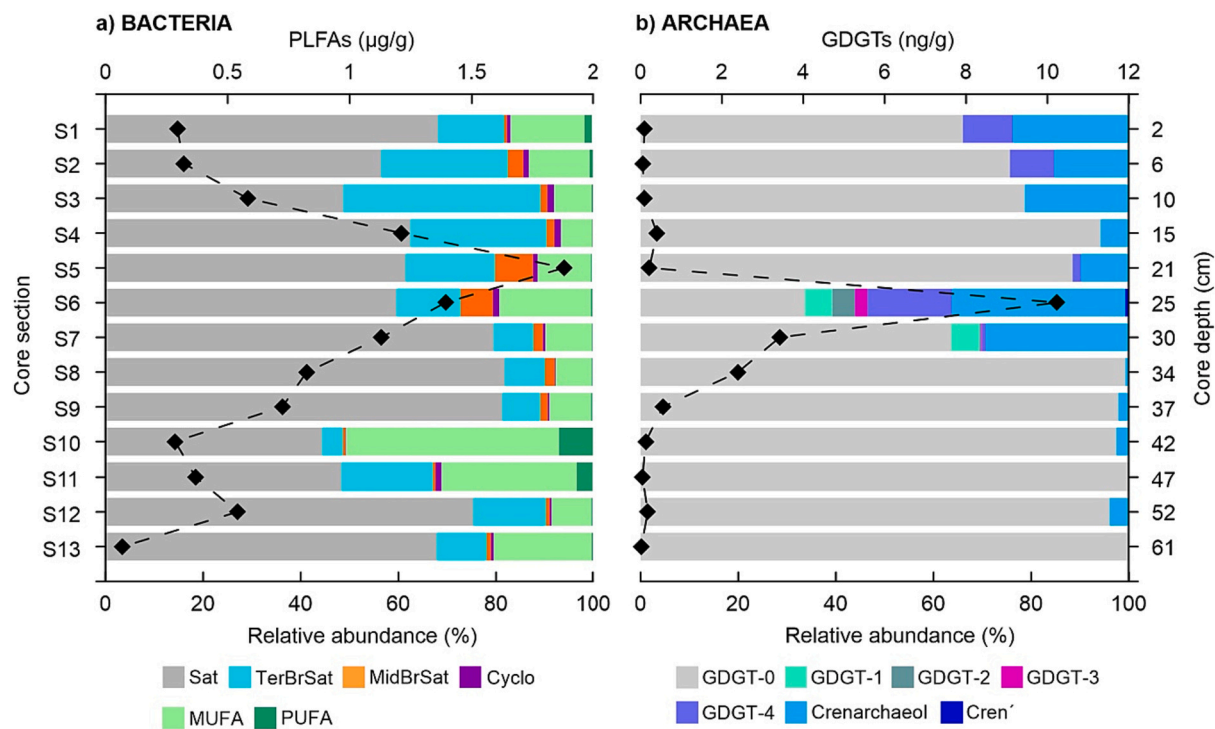
Fig. 5. Distribution and abundance of lipid biomarkers indicative of a) bacteria (PLFAs) and b) archaea (GDGTs) in sediments from distinct depth intervals (S1-S13) of the Rio Loa core. Total PLFA and GDGT concentrations are indicated as black diamonds.

Table 3

Abundance, molecular and hydrogen isotopic composition (δD) of the most abundant leaf wax *n*-alkanes detected in distinct depth/age intervals of the Rio Loa sediment core. Measurements were performed on sediment fractions (F < 1 mm; S1-S13) and the plant fractions (F > 1 mm; P6-P7), where enough material was available.

Sample ID	Depth (cm)	Age (yr cal BP)	Alkanes (ug/g)	ACL	CPI	*n*-C$_{23}$ δD (‰)	*n*-C$_{25}$ δD (‰)	*n*-C$_{27}$ δD (‰)	*n*-C$_{29}$ δD (‰)	*n*-C$_{31}$ δD (‰)
S1	2	40	0.07	27.9	2.3	−151 ± 3	−145 ± 3	−153 ± 3	−149 ± 3	−154 ± 3
S2	6	119	0.01	27.8	3.1	n.d.	n.d.	n.d.	n.d.	n.d.
S3	10	198	0.17	27.0	3.6	−156 ± 1	−159 ± 2	−164 ± 2	−167 ± 1	−170 ± 1
S4	15	294	0.26	26.9	3.6	−148 ± 4	−154 ± 2	−156 ± 2	−157 ± 0	−155 ± 2
S5	21	464	0.52	27.3	2.9	−141 ± 2	−156 ± 0	−162 ± 0	−145 ± 0	−156 ± 0
S6	25	556	0.43	26.9	3.4	−153 ± 1	−156 ± 0	−157 ± 2	−157 ± 1	−155 ± 1
S7	30	695	0.56	27.5	2.9	−154 ± 0	−158 ± 0	−160 ± 0	−160 ± 1	−163 ± 0
S8	34	798	0.30	27.9	2.7	−155 ± 1	−158 ± 2	−162 ± 1	−164 ± 1	−168 ± 1
S9	37	846	0.25	27.6	2.8	−160 ± 1	−164 ± 1	−170 ± 1	−166 ± 0	−168 ± 0
S10–11	45	998	0.08	27.5	3.3	−151 ± 3	−164 ± 3	−163 ± 3	−162 ± 3	−165 ± 3
S12	52	1124	0.16	27.0	3.3	−160 ± 2	−166 ± 1	−166 ± 1	−165 ± 1	−161 ± 0
S13	61	1329	0.02	27.0	2.0	n.d.	n.d.	n.d.	n.d.	n.d.
P6	25	556	3.8	27.6	6.6	−147 ± 1	−149 ± 2	−154 ± 1	−159 ± 1	−166 ± 1
P7	30	695	22.9	27.4	6.4	−148 ± 1	−154 ± 2	−160 ± 1	−161 ± 1	−161 ± 3

n.d. = not determined.

Average Chain Length (ACL) = Σ(Cn × n) / Σ(n), where C$_n$ is the abundance of each *n*-alkane with n carbon atoms for chain lengths from C$_{23}$ to C$_{33}$.

Carbon Preference Index (CPI) = 0.5 × [(Σ even/ Σ odd) + (Σ even/ Σ odd)].

Samples S10 and S11 were combined due to very low *n*-alkane abundances.

chronological information is often missing, and the development of robust age-depth models is often a challenge due to scarce plant remains, extremely low organic C contents and usually discontinuous deposition and low resolution (Finstad et al., 2018; Jaeschke et al., 2019; Ritter et al., 2019; Wennrich et al., 2023). The dune archive investigated in this study provides a unique record of paleoenvironmental history over the last ~1300 years (Figs. 2, 6). Distinct layers of fossil *Tillandsia* biomass buried in the dune suggest that plant growth occurred periodically until approximately 310 cal yr BP (Table 1). This is generally consistent with previous studies from other extinct *Tillandsia* dune fields spanning longer timescales of up to ~3500 years (Latorre et al., 2011; Jaeschke et al., 2019). While those studies focused on the buried plant material recovered from the dunes, the sedimentary units also provide important

information on past dune development, local depositional environments as well as substantial evidence of environmental changes (Fig. 2).

The texture of the sediment is largely controlled by the aeolian input of silt- to sand-sized particles, with fine sand being the dominant fraction. The well-rounded sand grains (Supplementary Fig. 3), typical for aeolian transport, together with a similar mineralogical content in the sediment core point to the same sediment source and transport trajectories to the dune location by prevailing winds from the west-southwest (Fig. 1b). The dune deposit, required as stabilizing substrate for the plants (Latorre et al., 2011; Koch et al., 2020), shows a surprisingly homogeneous grain size distribution particularly in the upper part of the core (0–39 cm b.s.) but also between 49 and 53 cm b.s., where plant material is abundant (Fig. 2). This indicates a relatively stable
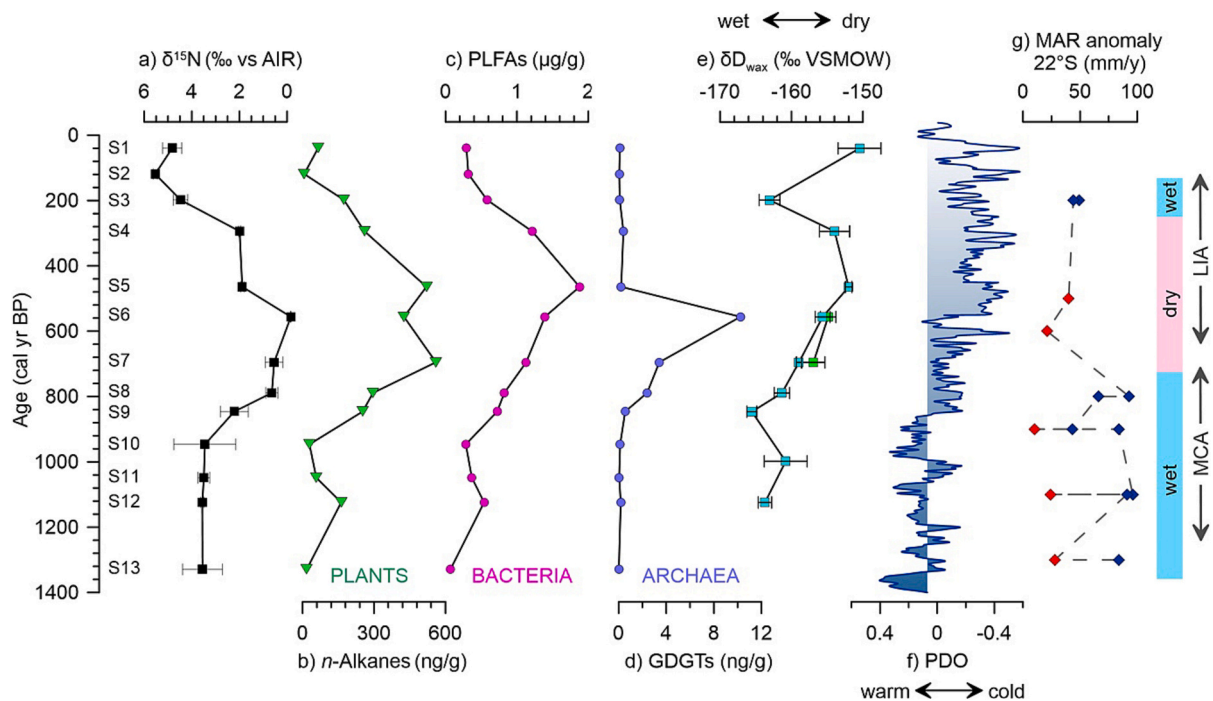
Fig. 6. Changes in paleoclimate, plant distribution, microbial abundances and nitrogen cycle during the past ~1300 years. Downcore variation of (a) $\delta^{15}N$, lipid biomarkers of (b) higher plants, (c) bacteria, and (d) archaea, together with (e) hydroclimate variability based on δD_{wax} in sediments (blue squares) and plant fragments (green squares), (f) shifts in Pacific Decadal Oscillation (PDO), representing long-lived pattern of sea surface temperature anomalies (Mantua et al., 1997; Mann et al., 2009) as well as (g) central Atacama rainfall anomalies estimated from paleomiddens (González-Pinilla et al., 2021). MCA = Medieval Climate anomaly; LIA = Little Ice Age. S1-S13 refers to the individual core sections. (For interpretation of the references to colour in this figure legend, the reader is referred to the web version of this article.)

depositional regime related to the presence of living *Tillandsia*, resulting in the accumulation of poorly sorted fine sand with minor components of medium and coarse sand and clay and silt contents of ~2 and ~ 8%, particularly prevailing during the past ~700 years. In contrast, the lower part of the core (~39–67 cm b.s.) is characterized by a more variable grain size distribution with higher medium to coarse sand contents. In general, textural differences, notably a higher sand content (>90%) compared to dunes of the Llamara Basin to the north-northeast (Finstad et al., 2018), likely reflect slightly different wind dynamics such as higher wind speeds in the direct vicinity of the Rio Loa canyon, and/ or point to different sediment sources and sediment source distances for the dune deposits investigated here. Higher wind speeds could increase both, the size of sand grains and erosion from the dune (Finstad et al., 2018), which can be inferred from distinct horizons at ~39–44 cm b.s. (ca. 900–1000 cal yr BP) and at the surface characterized by coarse sand (Fig. 2; Supplementary Fig. 2c). While these horizons can be interpreted as periods or single events with increased wind speeds, it seems that this lower core section reflects a period of fluctuating depositional conditions at the coring site, during which colonization by *T. landbeckii* began, and the resulting dune field, or at least its lower part, was established. Particularly the sharp contact between the fine grained and Cl-enriched layer at ~45 cm b.s. (Fig. 2) and the subsequent normally graded coarse sand layer at ~39–44 cm b.s. suggests erosion of older, possibly *Tillandsia*-bearing horizons. Given the similarity of the sediments of this layer to the large wind ripples in the surroundings of the dune field (Supplementary Fig. 2), this may have been related to the presence of large wind ripples at the coring site, after the first *Tillandsia* plants (~49–53 cm b.s., ca. 1100 cal yr BP) had colonized the site.

One way to investigate changes in hydrological conditions is the use of leaf wax compounds and their hydrogen isotope composition (i.e., Schefuß et al., 2005). Leaf wax compounds such as long-chain *n*-alkanes are major lipid components of the cuticular wax layer of terrestrial higher plants, providing a protective barrier against water loss and UV-

radiation (Eglinton and Hamilton, 1967). Globally, site-averaged δD_{wax} values are positively correlated with precipitation δD (δD_p) values, indicating that δD_p is the dominant control on δD_{wax} (Sachse et al., 2012; Ladd et al., 2021). However, secondary factors such as vegetation type, photosynthetic pathway, and evapotranspiration as well as environmental parameters may impact δD_{wax}, sometimes complicating a straightforward interpretation of the paleohydrological proxy (Sachse et al., 2012). CAM plants such as *Tillandsia* are relatively rare compared to C_3 plants and found to inhabit diverse niches within the tropics (Lüttge, 2010). In consequence, only few studies have investigated δD_{wax} in CAM plants (Sternberg et al., 1984; Feakins and Sessions, 2010a, 2010b). Thus, the response of δD_{wax} to changes in δD_p in extremely arid regions and on larger spatio-temporal scales remains to be explored. The leaf wax composition of *T. landbeckii*, with an almost even distribution of *n*-alkanes in the range of C_{23}-C_{31} (Supplementary Fig. 7), was found to be quite unusual for desert plants but may relate to the specific plant type (Contreras et al., 2022). A recent study by Jaeschke et al. (2024) analyzed δD_{wax} in the same set of living *T. landbeckii* specimens along environmental gradients in the coastal Atacama Desert. The results indicate that site-averaged δD_{wax} values reflect the balance of precipitation (or in this case, fog amount) and evaporation, i.e., air relative humidity, and largely follow changes in δD_p even at the dry limit. Based on the findings of Jaeschke et al. (2024), we used δD_{wax} as a proxy for past hydroclimatic conditions in the study area, which reveals a considerable degree of variation of up to 15‰ (Fig. 6e). We interpret these variations in δD_{wax} such as D-depleted values indicate more humid conditions, while D-enriched values point to drier conditions, akin to an 'amount' effect.

Our record spans >1000 years and includes several major periods of centennial scale climate change, including the Medieval Climate Anomaly (MCA) and the Little Ice Age (LIA) (i.e., Mann et al., 2009). The resulting variation in δD_{wax} from our record shows changes similar to these major periods on multidecadal to centennial timescales (Fig. 6e-g).

Both MCA and LIA are well recognized in the Northern Hemisphere (NH), whereas the existence of these in the Southern Hemisphere (SH) and the level of synchronicity with the NH is still a controversial issue (Mann et al., 2009; Lüning et al., 2019; Neukom et al., 2019). Some studies from South America indicate a warm MCA and cold LIA, however, these records are predominantly derived from the high-altitude Andean mountains, which receive moisture from the Atlantic Ocean (i. e., Lüning et al., 2019). Late Holocene hydroclimate changes in the Atacama and adjacent Altiplano appear to be more complex, and are thought to be driven mostly by regime shifts in the El Niño Southern Oscillation (ENSO) (Olson et al., 2020; González-Pinilla et al., 2021; Jara et al., 2022). For example, rainfall anomalies estimated for the central Atacama using changes in rodent body sizes from paleomiddens have been attributed to internal variability forcing (i.e., ENSO regime shifts) with large positive anomalies during the MCA and negative anomalies at the onset of the LIA, which then becomes much wetter ca. 200 cal yr BP (Fig. 6g; modified after González-Pinilla et al., 2021). In contrast, lake pollen records from the Chilean Altiplano suggest either drier climate conditions or very little change during the MCA (Jara et al., 2020). ENSO is also a major driver of fog/low clouds in coastal northern Chile <25°S during positive/warm ENSO years (El Niño), while the reversed pattern is observed to the south (Garreaud et al., 2008). Del Rio et al. (2021) estimated about 50% higher fog frequencies during positive ENSO years, particularly during austral summer (19–21°S). Higher summer sea surface temperature (SST) of ca. +2 °C during strong El Niño years causes a greater stratocumulus cloud cover (Del Rio et al., 2021), which in turn lowers evaporative enrichment during the dry season. In contrast, reduced fog/low clouds occur during negative/cold ENSO years (La Niña), which impacts ecosystems along the coast by severely reducing water supply for the plants (Del Rio et al., 2021).

Our δD_{wax} record shows very clear long-term fluctuations in the intensity of wet and dry phases with an overall trend towards higher values throughout the sequence (Fig. 6e). These fluctuations appear to be related to a multidecadal mode of variability of the ocean-atmosphere system in the Pacific Basin, the Pacific Decadal Oscillation (PDO; Fig. 6f) (Mann et al., 2009; Schulz et al., 2011). As opposed to the ENSO inter-annual timescale, the PDO affects SSTs on longer timescales of 20–30 years (Mantua et al., 1997; Trenberth and Fasullo, 2013; Del Rio et al., 2021). During the positive phase of the PDO, enhanced surface warming is observed, whereas the negative phase of the PDO is associated with surface cooling (Trenberth and Fasullo, 2013). Since the mid-1970s, this index has been mostly positive again, but a reversal in recent decades to a negative PDO phase is one proposed driver for the persistent decline in vegetation in the coastal Atacama Desert (Schulz et al., 2011; Muñoz et al., 2016), which is also observed at low elevations in our study area (Fig. 1). Our δD_{wax} record indicates that dune growth was established during a generally more humid climate, but that most plant biomass was generated during a generally drier climate with less moisture (Fig. 6e). A decrease in fog events associated with a trend towards a positive phase of the PDO (Fig. 6f) may have led to the extinction of the active *T. landbeckii* dune north of the Rio Loa. These findings agree with the dieback of other low-elevation (<1000 m) relict *Tillandsia* fields, such as that present at Cerro Pajonales (c. 100 km to the north, Latorre et al., 2011) implying that an increase in cloud bank height or Marine Boundary Layer could also be another factor behind their demise.

4.2. Variations in past nutrient cycles within fog ecosystems

Besides water availability as the major agent for life, N concentrations influence the growth of plants, while plants in turn provide organic C and other resources for microorganisms. Both, plants and associated microbial communities have been reported to be involved in nutrient cycling even in hyperarid soils of the Atacama Desert (Jones et al., 2018; Knief et al., 2020; Fuentes et al., 2022). *T. landbeckii* is adapted to low water and nutrient availability as prevailing across the coastal Atacama Desert. As a consequence, the plants evolved a high N use efficiency,

which is reflected in high C/N ratios of up to 100–400 in the leaf tissue (González et al., 2011; Jaeschke et al., 2019; Alfaro et al., 2021). This creates a low-quality litter, which is not easily accessible for microorganisms, resulting in generally low rates of decomposition (Prieto et al., 2019; Alfaro et al., 2021). In the relict *T. landbeckii* dune C/N ratios of the plant fractions are much lower compared to living *T. landbeckii* plants from the same location (mean C/N ratio: 64; Jaeschke et al., 2019), likely resulting from increased degradation of the dead plant fragments particularly in the sediment. During periods of enhanced rainfall or in general more humid climate (Fig. 6e-g), more leaf litter would be available as nutrient source for microorganisms in the sediment (Jones et al., 2018; Prieto et al., 2019; Alfaro et al., 2021). Likewise, the lower abundance of long-chain *n*-alkanes and lower CPI values in the sediment compared to those of the plant fractions (Table 3) and living *T. landbeckii* (CPI: 7–11; Contreras et al., 2022) indicate microbial activity and enhanced recycling of plant organic matter in the sediments.

Changes in $\delta^{13}C$ can be used as indication of C sources and possibly processes acting in the sediment. For instance, microbial decomposition will result in ^{13}C-enriched organic C, while isotopically depleted CO_2 is respired (Bernhard et al., 2018; Knief et al., 2020). Furthermore, abiotic processes such as leaching can lead to ^{13}C-enrichment with age and depth (Philben et al., 2022). Vertical C transport by plant roots, which may shape $\delta^{13}C$ signatures in soil profiles (Philben et al., 2022), can be neglected as *T. landbeckii* lacks functional roots (Rundel et al., 1997). $\delta^{13}C$ values of C_3 plants or soils below C_3 vegetation in the Atacama Desert range between −21‰ and − 28‰ (Ehleringer et al., 1998; Díaz et al., 2016; Jaeschke et al., 2019; Knief et al., 2020). In contrast, the ^{13}C-enriched values (mean $\delta^{13}C$ of −12.6‰) of our plant fractions are in the typical range of CAM plants in the Atacama Desert (Ehleringer et al., 1998) and confirm earlier studies on *T. landbeckii* (Latorre et al., 2011; Jaeschke et al., 2019). The generally higher $\delta^{13}C$ values in the sediments (mean $\delta^{13}C$ of −10‰) suggest microbial decomposition. However, sedimentary $\delta^{13}C$ values of approximately −8‰ (Table 2) may also indicate the presence of carbonate (Quade et al., 2007). $\delta^{13}C$ values of +0.5‰ were reported in soils beneath living *T. landbeckii* plants (Alfaro et al., 2021), which is more comparable to $\delta^{13}C$ values of distinct carbonate layers associated with the plants (Latorre et al., 2011). Moreover, TC is much lower in the sediments compared to soils beneath living *T. landbeckii* (Alfaro et al., 2021), likely related to the lower contribution of inorganic C in the dune deposits.

Changes in sedimentary $\delta^{34}S$ values can be used to estimate the marine influence in areas along the coastal escarpment (Finstad et al., 2018). Biogenic marine sulfates have ^{34}S-enriched values of +13 to +22‰ (Bao et al., 2000), compared to anhydrite in the Soledad Formation, Llamara Basin, with $\delta^{34}S$ values of +6 ‰ (Finstad et al., 2018). As hyperarid deposits of the Atacama Desert consist primarily of anhydrite and gypsum (Finstad et al., 2018; Voigt et al., 2020; Knief et al., 2020), we may assess relative inputs of marine fog at our study site. Our sedimentary $\delta^{34}S$ values (Table 2) are about 2–3‰ more positive compared to sulfate $\delta^{34}S$ values of nearby dune deposits from the Llamara Basin (Finstad et al., 2018). With predominant winds from the west (Fig. 1b), a contribution of marine inputs via fog deposition is likely (Finstad et al., 2018). Surprisingly, while $\delta^{34}S$ did not exhibit much variation in the dune core (ca.1‰; Table 2), both S and $\delta^{34}S$ may contribute to shaping microbial community composition in the upper (S1-S4) and possibly the lower (S8) core sections (Fig. 4c). However, further in-depth analyses are required for more detailed information on biological sulfate cycling (Klipsch et al., 2023).

Globally, climate controls on the N cycle are suggested by the inverse relationship between foliar $\delta^{15}N$ and mean annual precipitation (i.e., Amundson et al., 2003). Previous studies analyzed foliar $\delta^{15}N$ in plant layers from excavated dunes and reported extremely ^{15}N-depleted values in relict *T. landbeckii* plant fragments compared to living plants near the site today (Latorre et al., 2011; Jaeschke et al., 2019), which we can confirm in our study (Supplementary Table 1). Such negative $\delta^{15}N$

values are not expected in hyperarid regions (i.e., Díaz et al., 2016) and are not comparable to global patterns of soil/plant $\delta^{15}N$ distributions based on C_3/C_4 plants (e.g., Amundson et al., 2003) but may relate to water and nutrient inputs from marine fog (Soderberg, 2010; Latorre et al., 2011; Jaeschke et al., 2019). In fog ecosystems, water and nutrient cycles are intrinsically linked to each other, thus considerable variations in foliar $\delta^{15}N$ along environmental gradients suggest that other factors than water amount may impact $\delta^{15}N$ in this hyperarid region, i.e., the marine N cycle and N inputs via fog deposition (González et al., 2011; Latorre et al., 2011; Jaeschke et al., 2019). The similar pattern of $\delta^{15}N$ and *n*-alkane abundances in the core (Fig. 6) may therefore primarily reflect plant $\delta^{15}N$ dynamics. In contrast, the diverging patterns in sedimentary $\delta^{15}N$ and δD_{wax} that were apparent in our core (Fig. 6), may be explained by microbial N dynamics affecting the $\delta^{15}N$ trend seen in our record (Supplementary Fig. 9). An important role of microbes in N cycling, either as free-living soil microorganisms or associated with plants has been pointed out for hyperarid regions (Díaz et al., 2016; Alfaro et al., 2021). The N cycle integrates many ecological inputs and outputs such as ammonification, nitrification and denitrification, all of them associated with extreme fractionation during mineralization (Robinson, 2001; Díaz et al., 2016). Environmental drivers, i.e., water availability, can contribute to ecosystem N fluxes, especially if microbes are involved (Robinson, 2001). On the other hand, N losses in arid areas can be caused by enhanced ammonia volatilization, due to cycles of wetting and drying at high pH values (>7) and associated with carbonates (Aranibar et al., 2004; Díaz et al., 2016). Thus, $\delta^{15}N$ as an integrator of N cycle processes in the dune is shaped by biotic factors, i. e., plant cover and microbial community composition, and abiotic factors, i.e., climate state and water inputs as proposed by Díaz et al. (2016).

4.3. Relict Tillandsia landbeckii dune as habitat for microorganisms

Despite the extreme environmental conditions prevailing in the study area, we found evidence for abundant and diverse microbial populations in the dune (Figs. 3–6). Only low yields of DNA and lipid biomarkers have been isolated and analyzed in previous studies from the hyperarid core of the Atacama Desert, mostly barren landscapes without any vegetation, revealing scarce microbial communities with low diversity dominated by *Actinobacteria*, *Proteobacteria* and *Firmicutes* (Navarro-González et al., 2003; Connon et al., 2007; Crits-Christoph et al., 2013; Azua-Bustos et al., 2015; Knief et al., 2020; Fuentes et al., 2022). In contrast, bacterial communities of surprisingly high diversity were recently detected either directly associated with *T. landbeckii* (Hakobyan et al., 2023) or in soils beneath the living plants (Alfaro et al., 2021). Hence, *T. landbeckii* may serve as important refugium for rich bacterial life in an otherwise hostile environment (Hakobyan et al., 2023). This is also indicated in our dune record, where microbial biomass is largely related to the presence/absence of *T. landbeckii* plant material (Figs. 2, 4, 6). The differences in community composition we detected in our core compared to those associated with below-ground shoots (laimosphere) of *Tillandsia* plants (Hakobyan et al., 2023) or the soil below plants (Alfaro et al., 2021) may be explained by small-scale habitat differentiation as well as high spatial variability in general, as observed between individual specimens from the same field. It may also relate to the specific environmental condition at the geographic location of the dune ecosystem, notably seasonal differences in fog availability, providing moisture and nutrients as well as wind strength and dust supply (González et al., 2011; Azua-Bustos et al., 2019; Alfaro et al., 2021; Hakobyan et al., 2023).

Aeolian transport of viable microbial cells has been shown in transects from the coast near Tocopilla and Iquique further inland (Azua-Bustos et al., 2019). Interestingly, the predominant species isolated from dust samples in that study belonged to *Bacillus*, which are spore-forming bacteria, some of them also of marine origin (Azua-Bustos et al., 2015, 2019). Therefore, a fraction of the species detected in our samples may

have traversed with dust or fog and arrived as spores to the dune location. Even though members of the *Firmicutes/Bacilli* were found to be common part of the bacterial community colonizing *T. landbeckii* (Alfaro et al., 2021; Hakobyan et al., 2023), the dominance in sand-dominated parts of our dune record is striking (Fig. 4a). A possible explanation might be that after the dune became extinct, the plants may still have acted as dust collectors, thus subsequently increasing the absolute amounts of *Bacilli* in the upper ~25 cm of the core, which was once surface covered by living *T. landbeckii* (Fig. 2). Thus, the predominance of *Bacilli* in the lower core section (S10-S13) may indicate that this part of the dune was also a former surface or hardground, possibly related to a different growth cycle of the dune. This is also suggested by the change in mineralogy of that core section around 40–45 cm b.s. with a distinct white layer (Fig. 2), and the extremely low abundance of plant fragments and *n*-alkanes (Figs. 2, 6b). Due to their spore forming capability, this group may particularly well survive throughout the core, leading to its dominance in layers that do otherwise not support a rich microbial life.

Actinobacteria, the predominant class detected in soils beneath living *T. landbeckii* (70.5%; Alfaro et al., 2021) and along an elevation transect near Quebrada Aroma (Knief et al., 2020), were less abundant in the dune record from the Rio Loa canyon (Fig. 4a), and also highly variable in both, phyllosphere and laimosphere of *T. landbeckii* (Hakobyan et al., 2023). However, highest abundances of ca. 10–20% were also found below the layer with highest yield of plant fragments, pointing to a distinct microhabitat in the deeper part of the dune record, possibly related to the initial growth cycle of *T. landbeckii* during a generally more humid climate (Fig. 6e-g). A distinct class of *Actinobacteria*, i.e., *Rubrobacteria* has been detected as widespread and dominant colonizer of desert soils (Connon et al., 2007; Crits-Christoph et al., 2013; Knief et al., 2020), which would be in line with our interpretation. Members of the *Bacteroidetes* and *Proteobacteria*, observed to be related to higher moisture content along the aridity transect near Quebrada Aroma (Knief et al., 2020), dominated the more diverse microbial community in the central part of the dune record (Fig. 4a), in accordance with the bacterial colonizer community of the living plants (Hakobyan et al., 2023). This is largely associated with the distribution of C and N (S5-S7; Fig. 4c) and may thus relate to the higher amount of nutrients released by plant litter during a generally more humid climate compared to the upper part of the core (Fig. 6b). For the microbes below this layer, nutrients may become available due to leaching and downward transport upon irregular heavy rainfall events, i.e., during El Niño years, thereby sustaining a smaller though still viable microbial population that is capable of alternating between active and inactive states (Jones et al., 2018; Schulze-Makuch et al., 2018; Rosinger et al., 2023). Activation of the microbial community and subsequent mineralization of high molecular weight C substrates has been shown for soils of the Atacama Desert along an aridity gradient (Jones et al., 2018). In contrast, more arid conditions prevailing throughout most of the LIA (Fig. 6e-g) may have slowed down internal C and N cycling indicated by reduced bacterial biomass in the upper part of the core (Fig. 6c, d).

While *T. landbeckii* was suggested to be inhabited by viable microorganisms (Hakobyan et al., 2023), this is less evident from the relict dune. DNA and even more so PLFAs are indicative of viable cells but cannot distinguish between active and dormant cells. Both may even reflect a certain fossil component, especially if preservation of dead cells is high due to extremely low water activity in hyperarid soils (Connon et al., 2007; Wilhelm et al., 2017; Frindte et al., 2020). Metabolically active stressed or starved populations, mostly gram-negative bacteria, are known to convert certain PLFAs to trans- and cyclic compounds (Heipieper et al., 1996; Pinkart et al., 2002; Lester et al., 2007). The presence of these markers at low abundances is thus indicative of metabolic activity, particularly in the upper part of the core, and is largely consistent with the distribution of CFUs (Fig. 3; Supplementary Fig. 8). Higher aridity and low litter content (or poor litter quality of the plant remains) may induce stress, while an absence of these markers

indicate that negligible metabolic activity has occurred (i.e., stasis) as shown for the most arid sites Yungay and Maria Elena South (Connon et al., 2007; Rosinger et al., 2023). Cell numbers observed in the dune core are much higher compared to hyperarid soils from Yungay and Maria Elena South (Connon et al., 2007; Shen et al., 2019), but are comparable to those from surface soils near Quebrada Aroma (Knief et al., 2020), which belongs to the arid Precordillera of the Andes and receives higher precipitation amounts of ca. 10–40 mm/yr with increasing elevation (Mörchen et al., 2021). CFUs are likewise in the range of those reported for the transition zones from hyperarid to arid soils in the southern Atacama Desert (Shen et al., 2019). The accumulation of living cells mostly in the upper layers of the dune might be explained by water availability along with possible differences in plant N content (higher plant to soil ratio; Supplementary Table 1) in comparison to older deeper layers. A drier climate during most of the LIA (Fig. 6e-g) may have led to enhanced dry deposition, causing nitrate accumulation and a slight drop in pH (Wang et al., 2014) and maybe more favourable conditions for members of the *Firmicutes* to stay dormant but viable, which is indicated by both 16S rRNA genes and the high abundance of terminally branched PLFAs (Figs. 4a, 5a).

Archaea have not been detected consistently in soils/sediments of the Atacama Desert (Crits-Christoph et al., 2013; Azua-Bustos et al., 2015, 2019), which may relate to in general low abundances and their patchy spatial distribution (Wilhelm et al., 2017; Knief et al., 2020; Hwang et al., 2021; Rosinger et al., 2023). Ammonia-oxidizing *Thaumarchaeota* (AOA group 1.1.b; *Nitrososphaera* lineage) were recently detected sheltered below boulders covering surface soils of the hyperarid core of the desert, pointing to their occurrence in more restricted ecological niches than bacteria and revealing a surprisingly high adaptability and resilience (xerotolerance) to the extreme desert conditions (Hwang et al., 2021). Predominance of 'Candidatus Nitrosocosmicus', which belongs to terrestrial AOA, in dune layers S6 and S7 (Supplementary Fig. 6) together with distinct compositional changes of GDGTs (Fig. 5b) point to a more favourable microhabitat for *Thaumarchaeota* at these depth intervals. Here, both bacterial and plant biomass are also high as indicated by PLFAs and *n*-alkanes, respectively (Fig. 6). Hence, these microbes are likely being influenced by increasing supplies of both C and ammonia (Jung et al., 2014; Hwang et al., 2021), which is released upon decomposition of dead organic matter (i.e., high microbial turnover). In contrast, reduced plant litter and bacterial biomass and thus available C in the deeper part of the sediment core (S10–13) may explain the change in archaeal abundance and community composition towards *Euryarchaeota* (Supplementary Fig. 6). N nutrients as a source for biomass production and energy source for chemotrophic metabolisms may be provided by increased sedimentary plant litter (Supplementary Fig. 9a) and potentially also by solubilization and downward transport of atmospherically-derived nitrate during rare but intense rainfall events (Alfaro et al., 2021; Prieto et al., 2019; Shen et al., 2019). A potential role in N cycling is also indicated by the correlation of $\delta^{15}N$ and archaeal GDGTs in the central part of the dune core (Supplementary Fig. 9d).

5. Conclusions

In this study, a comprehensive set of physical, chemical, microbial and lipid biomarker analyses was applied in a sediment core from the coastal Atacama Desert to investigate the links between hydroclimate evolution, *Tillandsia* dune growth and microbial abundance and diversity over the past ~1300 years. Our coring enabled more detailed research into the intact and stratified dune archive at higher temporal resolution compared to previous studies. The unique dune record provided a first snapshot of past hydroclimatic conditions in the study area. Based on the distribution of plant remains and δD_{wax} we suggest that *T. landbeckii* colonization was initiated during a generally more humid climate (MCA) than today, but that dune formation continued during most of the LIA, even at higher aridity, until the ecosystem finally died

off due to lack of sufficient fog water. The pattern of δD_{wax} variability is in line with a shift from positive to negative PDO as well as precipitation anomalies in the area. The observed multidecadal changes in δD_{wax} are also consistent with the extremely slow growth rates of the plants, so that δD_{wax} reflects a time-integrated signal of hydrological changes. The unique *Tillandsia* dune ecosystem harbours a microbial community composed of bacterial and archaeal groups, that would otherwise not occur in this extreme environment with the observed population size and diversity. The plants provide important resources and generate microhabitats for specific microbial groups, such as nitrifying *Thaumarchaeota*. Furthermore, these isolated dune ecosystems seem to be hotspots for enhanced C and N cycling at the dry limit. It is likely that a large proportion of the microorganisms present in the dune are dormant, even at greater depths, and can be reactivated upon rewetting during infrequent rainfall events. Also, while there seems to be a direct coupling between plant occurrence and microbial abundance and diversity, a direct link between past climate evolution and microbial content remains ambiguous. Investigation of more dune archives will help to decipher whether these distinct microbial hotspots can be detected along larger spatiotemporal gradients.

Data availability

The 16S rRNA gene sequence reads generated in this study have been deposited in the European Nucleotide Archive (ENA) under accession no. PRJEB61789. All other data of this study will be made available at the CRC1211 database (https://www.crc1211db.uni-koeln.de).

Appendix A. Supplementary data

Supplementary data to this article can be found online at https://doi.org/10.1016/j.gloplacha.2024.104383.

References

Alfaro, F.D., Manzano, M., Almiray, C., García, J.L., Osses, P., Del Rio, C., Vargas, C., Latorre, C., Koch, M.A., Siegmund, A., Abades, S., 2021. Soil bacterial community structure of fog-dependent *Tillandsia landbeckii* dunes in the Atacama Desert. Pl. Syst. Evol. 307, 56. https://doi.org/10.1007/s00606-021-01781-0.

Amato, P., Menager, M., Sancelme, M., Laj, P., Mailhot, G., Delort, A.M., 2005. Microbial population in cloud water at the Puy de Dome: implications for the chemistry of clouds. Atmos. Environ. 39, 4143–4153.

Amundson, R., Austin, A.T., Schuur, E.A.G., Yoo, K., Matzek, V., Kendall, C., Uebersax, A., Brenner, D., Baisden, W.T., 2003. Global patterns of the isotopic composition of soil and plant nitrogen. Glob. Biogeochem. Cy. 17 (1), 1031.

Aranibar, J.N., Otter, L., Macko, S.A., Feral, C.J., Epstein, H.E., Dowty, P.R., Eckardt, F., Shugart, H.H., Swap, R.J., 2004. Nitrogen cycling in the soil-plant system along a precipitation gradient in the Kalahari sands. Glob. Chang. Biol. 10, 359–373. https://doi.org/10.1046/j.1529-8817.2003.00698.x.

Azua-Bustos, A., Urrejola, C., Vicuna, R., 2012. Life at the dry edge: microorganisms of the Atacama Desert. FEBS Lett. 586, 2939–2945.

Azua-Bustos, A., Caro-Lara, L., Vicuna, R., 2015. Discovery and microbial content of the driest site of the hyperarid Atacama Desert, Chile. Environ. Microbiol. Rep. 7, 388–394.

Azua-Bustos, A., Gonzalez-Silva, C., Fernandez-Martinez, M.A., Arenas-Fajardo, C., Fonseca, R., Martin-Torres, F.J., Fernandez-Sampedro, M., Fairen, A.G., Zorzano, M. P., 2019. Aeolian transport of viable microbial life across the Atacama Desert, Chile: implications for Mars. Sci. Rep. 9, 11024.

Bao, H., Campbell, D.A., Bockheim, J.G., Thiemens, M.H., 2000. Origins of sulphate in Antarctic Dry-Valley soils as deduced from anomalous ^{17}O compositions. Nature 407, 499–502.

Bernhard, N., Moskwa, L.-M., Schmidt, K., Oeser, R.A., Aburto, F., Bader, M.Y., Baumann, K., Blanckenburg, F., Boy, J., Brink, L., Brucker, E., Büdel, B., Canessa, R., Dippold, M.A., Ehlers, T.A., Fuentes, J.P., Godoy, R., Jung, P., Karsten, U., Köster, M., Kuzyakov, Y., Leinweber, P., Neidhardt, H., Matus, F., Mueller, C.W., Oelmann, Y., Oses, R., Osses, P., Paulino, L., Samolov, E., Schaller, M., Schmid, M., Spielvogel, S., Spohn, M., Stock, S., Stroncik, N., Tielbörger, K., Übernickel, K., Scholten, T., Seguel, O., Wagner, D., Kühn, P., 2018. Pedogenic and microbial interrelations to regional climate and local topography: new insights from a climate gradient (arid to humid) along the Coastal Cordillera of Chile. Catena 170, 335–355. https://doi.org/10.1016/j.catena.2018.06.018.

Blaauw, M., Christen, J.A., 2011. Flexible paleoclimate age-depth models using an autoregressive gamma process. Bayesian Anal. 6, 457–474.

Blott, S.J., Pye, K., 2001. GRADISTAT: a grain size distribution and statistics package for the analysis of unconsolidated sediments. Earth Surf. Process. Landf. 26, 1237–1248.

Böhm, C., Schween, J.H., Reyers, M., Maier, B., Löhnert, U., Crewell, S., 2021. Toward a Climatology of fog Frequency in the Atacama Desert via Multispectral Satellite Data and Machine Learning Techniques. J. Appl. Meteorol. Climatol. 60, 1149–1169. https://doi.org/10.1175/JAMC-D-20- 0208.s1.

Bolyen, E., Rideout, J.R., Dillon, M.R., Bokulich, N., Abnet, C.C., Al-Ghalith, G.A., 2019. Reproducible, interactive, scalable and extensible microbiome data science using QIIME 2. Nat. Biotechnol. 37 (8), 852–857.

Borthagaray, A.I., Fuentes, M.A., Marquet, P.A., 2010. Vegetation pattern formation in fog-dependent ecosystem. J. Theoret. Biol. 265, 18–26.

Callahan, B.J., McMurdie, P.J., Rosen, M.J., Han, A.W., Johnson, A.J.A., Holmes, S.P., 2016. DADA2: High-resolution sample inference from Illumina amplicon data. Nat. Methods 13 (7), 581.

Caporaso, J.G., Lauber, C.L., Walters, W.A., Berg-Lyons, D., Lozupone, C.A., Turnbaugh, P.J., 2011. Global patterns of 16S rRNA diversity at a depth of millions of sequences per sample. Proc. Natl. Acad. Sci. USA 108, 4516–4522.

Cereceda, P., Larrain, H., Osses, P., Farías, M., Egaña, I., 2008. The spatial and temporal variability of fog and its relation to fog oases in the Atacama Desert, Chile. Atmos. Res. 87, 312–323. https://doi.org/10.1016/j.atmosres.2007.11.012.

Connon, S.A., Lester, E.D., Shafaat, H.S., Obenhuber, D.C., Ponce, A., 2007. Bacterial diversity in hyperarid Atacama Desert soils. J. Geophys. Res. 112 https://doi.org/10.1029/2006JG000311.

Contreras, S., Landahur, M., García, K., Latorre, C., Reyers, M., Rethemeyer, J., Jaeschke, A., 2022. Leaf wax composition and distribution of Tillandsia landbeckii reflects moisture gradient across the hyper-arid Atacama Desert. Pl. Syst. Evol. 308, 8. https://doi.org/10.1007/s00606-021-01800-0.

Crits-Christoph, A., Robinson, C.K., Barnum, T., Fricke, W.F., Davila, A.F., Jedynak, B., McKay, C.P., DiRuggiero, J., 2013. Colonization patterns of soil microbial communities in the Atacama Desert. Microbiome 1, 28. https://doi.org/10.1186/2049- 2618-1-28.

Del Rio, C., Lobos-Roco, F., Latorre, C., Koch, M.A., Garcia, J.L., Osses, P., Lambert, F., Alfaro, F., Siegmund, A., 2021. Spatial distribution and interannual variability of coastal fog and low clouds cover in the hyperarid Atacama Desert and implications for past and present *Tillandsia landbeckii* ecosystems. Pl. Syst. Evol. 58, 1–23. https://doi.org/10.1007/s00606-021-01782-z.

Díaz, F.P., Frugone, M., Gutiérrez, R.A., Latorre, C., 2016. Nitrogen cycling in an extreme hyperarid environment inferred from δ^{15}N analyses of plants, soils and herbivore diet. Sci. Rep. 6, 22226. https://doi.org/10.1038/srep22226.

Dirks, I., Navon, Y., Kanas, D., Dumbur, R., Grunzweig, J.M., 2017. Atmospheric water vapor as driver of litter decomposition in Mediterranean shrubland and grassland during rainless seasons. Glob. Chang. Biol. 16, 2799–2812.

Dueker, M.E., O'Mullan, G.D., Weathers, K.C., Juhl, A.R., Uriarte, M., 2012. Coupling of fog and marine microbial content in the near-shore coastal environment. Biogeosciences 9, 803–813.

Dunai, T.J., Gonzalez Lopez, G.A., Juez-Larre, J., 2005. Oligocene-Miocene age of aridity in the Atacama Desert revealed by exposure dating of erosion- sensitive landforms. Geology 33, 321–324.

Eglinton, G., Hamilton, R.J., 1967. Leaf epicuticular waxes. Science 156, 1322.

Ehleringer, J.R., Rundel, P.W., Palma, B., Mooney, H.A., 1998. Carbon isotope ratios of Atacama Desert plants reflect hyperaridity of region in northern Chile. Rev. Chil. Hist. Nat. 71, 79–86.

Evans, S.E., Dueker, M.E., Logan, J.R., Weathers, K.C., 2019. The biology of fog: results from coastal Maine and Namib Desert reveal common drivers of fog microbial composition. Sci. Total Environ. 647, 1547–1556. https://doi.org/10.1016/j.scitotenv.2018.08.045.

Feakins, S.J., Sessions, A.L., 2010a. Controls on the D/H ratios of plant leaf waxes from an arid ecosystem. Geochim. Cosmochim. Acta 74, 2128–2141.

Feakins, S.J., Sessions, A.L., 2010b. Crassulacean acid metabolism influences D/H ratio of leaf wax in succulent plants. Org. Geochem. 41, 1269–1276. https://doi.org/10.1016/j.orggeochem.2010.09.007.

Finstad, K.M., Pfeiffer, M., McNicol, G., Tuite, M., Williford, K., Amundson, R., 2018. A late Quaternary paleoenvironmental record in sand dunes of the northern Atacama Desert, Chile. Quat. Res. 90, 127–138. https://doi.org/10.1017/qua.2018.20.

Folk, R.L., Ward, W.C., 1957. A Study in the significance of Grain-size Parameters. J. Sediment. Petrol. 27, 3–26.

Frindte, K., Pape, R., Werner, K., Loffler, J., Knief, C., 2019. Temperature and soil moisture control microbial community composition in an arctic-alpine ecosystem along elevational and micro-topographic gradients. ISME J. 13 (8), 2031–2043.

Frindte, K., Lehndorff, E., Vlaminck, S., Werner, K., Kehl, M., Khormali, F., Knief, C., 2020. Evidence for signatures of ancient microbial life in paleosols. Sci. Rep. 10, 16830. https://doi.org/10.1038/s41598-020-73938-9.

Fuentes, B., Choque, A., Gómez, F., Alarcón, J., Castro-Nallar, E., Arenas, F., Contreras, D., Mörchen, R., Amelung, W., Knief, C., Moradi, G., Klumpp, E., Saavedra, C.P., Prietzel, J., Klysubun, W., Remonsellez, F., Bol, R., 2022. Influence of Physical-Chemical Soil Parameters on Microbiota Composition and Diversity in a Deep Hyperarid Core of the Atacama Desert. Front. Microbiol. 12, 794743 https://doi.org/10.3389/fmicb.2021.794743.

García, J.L., Lobos-Roco, F., Schween, J.H., Del Rio, C., Osses, P., Vives, R., Pezoa, M., Siegmund, A., Latorre, C., Alfaro, F., Koch, M.A., Loehnert, U., 2021. Climate and coastal low-cloud dynamic in the hyperarid Atacama fog Desert and the geographic distribution of Tillandsia landbeckii (Bromeliaceae) dune ecosystems. Pl. Syst. Evol. 307, 57. https://doi.org/10.1007/s00606-021-01775-y.

Garreaud, R., Barichivich, J., Christie, D., Maldonado, A., 2008. Interannual variability of the coastal fog at Fray Jorge relict forests in semiarid Chile. J. Geophys. Res. 113, G04011. https://doi.org/10.1029/2008JG000709.

Garreaud, R.D., Vuille, M., Compagnucci, R., Marengo, J., 2009. Present-day south American climate. Palaeogeogr. Palaeoclimatol. Palaeoecol. 281 (3–4), 180–195.

González, A.L., Fariña, J.M., Pinto, R., Pérez, C., Weathers, K.C., Armesto, J.J., Marquet, P.A., 2011. Bromeliad growth and stoichiometry: responses to atmospheric nutrient supply in fog-dependent eco- systems of the hyper-arid Atacama Desert, Chile. Oecologia 167, 835–845. https://doi.org/10.1007/s00442-011-2032-y.

González-Pinilla, F.J., Latorre, C., Rojas, M., Houston, J., Rocuant, M.I., Maldonado, A., Santoro, C.M., Quade, J., Betancourt, J.L., 2021. High- and low-latitude forcings drive Atacama Desert rainfall variations over the past 16,000 years. Sci. Adv. 7, eabg1333. https://doi.org/10.1126/sciadv.abg1333.

Hakobyan, A., Velte, S., Sickel, W., Quandt, D., Stoll, A., Knief, C., 2023. *Tillandsia landbeckii* phyllosphere and laimosphere as refugia for bacterial life in a hyperarid desert environment. Microbiome 11, 246. https://doi.org/10.1186/s40168-023-01684-x.

Haslam, R., Borland, A., Maxwell, K., Griffiths, H., 2003. Physiological responses of the CAM epiphyte Tillandsia usneoides L. (Bromeliaceae) to variations in light and water supply. J. Pl. Physiol. 160, 627–634. https://doi.org/10.1078/0176-1617-00970.

Heipieper, H.J., Meulenbeld, G., VanOirschot, Q., DeBont, J., 1996. Effect of environmental factors on the trans/cis ratio of unsaturated fatty acids in Pseudomonas putida S12. Appl. Environ. Microbiol. 62, 2773–2777.

Hoffmeister, D., 2018a. Meteorological and Soil Measurements of the Permanent Basis Weather Station 12 - Rio Loa, Chile. CRC1211 Database (CRC1211DB). https://doi.org/10.5880/CRC1211DB.3.

Hoffmeister, D., 2018b. Meteorological and Soil Measurements of the Permanent Master Weather Station 13 - Cerros de Calate, Chile. CRC1211 Database (CRC1211DB). https://doi.org/10.5880/CRC1211DB.4.

Hogg, A.G., Heaton, T.J., Hua, Q., Palmer, J.G., Turney, C.S.M., Southon, J., Bayliss, A., Blackwell, P.G., Boswijk, G., Bronk Ramsey, C., Petchey, F., Reimer, P., Reimer, R., Wacker, L., 2020. SHCal20 Southern Hemisphere Calibration, 0–55,000 years cal BP. Radiocarbon 62 (4), 759–778.

Hopmans, E.C., Schouten, S., Sinninghe Damsté, J.S., 2016. The effect of improved chromatography on GDGT-based palaeoproxies. Org. Geochem. 93, 1–6.

Houston, J., 2006. Variability of precipitation in the Atacama Desert: its causes and hydrological impact. Int. J. Climatol. 26, 2181–2198. https://doi.org/10.1002/joc.1359.

Houston, J., Hartley, A.J., 2003. The central Andean west-slope rain-shadow and its potential contribution to the origin of hyper-aridity in the Atacama Desert. Int. J. Climatol. 23, 1453–1464. https://doi.org/10.1002/joc.938.

Huguet, C., Hopmans, E.C., Febo-Ayala, W., Thompson, D.H., Sinninghe Damsté, J.S., Schouten, S., 2006. An improved method to determine the absolute abundance of glycerol dibiphytanyl glycerol tetraether lipids. Org. Geochem. 37, 1036–1041.

Hwang, Y., Schulze-Makuch, D., Arens, F.L., Saenz, J.S., Adam, P.S., Sager, C., Bornemann, T.L.V., Zhao, W., Zhang, Y., Airo, A., Schloter, M., Probst, A.J., 2021. Leave no stone unturned: individually adapted xerotolerant Thaumarchaeota

sheltered below the boulders of the Atacama Desert hyperarid core. Microbiome 9, 234. https://doi.org/10.1186/s40168-021-01177-9.

Jacobson, K., van Diepeningen, A., Evans, S., Fritts, R., Gemmel, P., Marsho, C., Seely, M., Wenndt, A., Yang, X., Jacobson, P., 2015. Non-rainfall moisture activates fungal decomposition of surface litter in the Namib sand sea. PLoS One 10 (5), e0126977. https://doi.org/10.1371/journal.pone.0126977.

Jaeschke, A., Böhm, C., Merklinger, F.F., Bernasconi, S.M., Reyers, M., Kusch, S., Rethemeyer, J., 2019. Variation in $\delta^{15}N$ of fog-dependent *Tillandsia* ecosystems reflect water availability across climate gradients in the hyperarid Atacama Desert. Glob. Planet. Chang. 183, 103029 https://doi.org/10.1016/j.glop.lacha.2019.103029.

Jaeschke, A., Böhm, C., Schween, J.H., Schefuß, E., Latorre, C., Contreras, S., Koch, M.A., Rethemeyer, J., Lücke, A., 2024. Evaluating the isotopic composition of leaf organic compounds in fog-dependent *Tillandsia landbeckii* across the coastal Atacama Desert: implications for hydroclimate reconstructions at the dry limit. Glob. Planet. Chang. https://doi.org/10.1016/j.gloplacha.2024.104393.

Jara, I.A., Maldonado, A., de Porras, M.E., 2020. Late Holocene dynamics of the south American summer monsoon: New insights from the Andes of northern Chile (21°S). Quat. Sci. Rev. 246, 106533 https://doi.org/10.1016/j.quascirev.2020.106533.

Jara, I.A., Maldonado, A., de Porras, M.E., 2022. Did modern precipitation drivers influence centennial trends in the highlands of the Atacama Desert during the most recent millennium? Geophys. Res. Lett. 49 https://doi.org/10.1029/2021GL095927 e2021GL095927.

Jones, D.L., Olivera-Ardid, S., Klumpp, E., Knief, C., Hill, P.W., Lehndorff, E., Bol, R., 2018. Moisture activation and carbon use efficiency of soil microbial communities along an aridity gradient in the Atacama Desert. Soil Biol. Biochem. 117, 68–71. https://doi.org/10.1016/j.soilbio.2017.10.026.

Jung, M.-Y., Park, S.-J., Kim, S.-J., Kim, J.-G., Sinninghe Damsté, J.S., Jeon, C.O., Rhee, S.-K., 2014. A mesophilic, autotrophic, ammonia-oxidizing archaeon of thaumarchaeal group I. 1a cultivated from a deep oligotrophic soil horizon. Appl. Environ. Microbiol. 80, 3645–3655.

Kaur, A., Chaudhary, A., Kaur, A., Choudhary, R., Kaushik, R., 2005. Phospholipid fatty acid – a bioindicator of environment monitoring and assessment in soil ecosystem. Curr. Sci. 89, 1103–1112.

Klipsch, S., Herwartz, D., Voigt, C., Münker, C., Chong, G., Böttcher, M.E., Staubwasser, M., 2023. Sulphate deposition, biologic cycling, and mobility in Atacama Desert soils revealed by sulphate isotope signatures. Glob. Planet. Chang. 230, 104290 https://doi.org/10.1016/j.gloplacha.2023.104290.

Knief, C., Bol, R., Amelung, W., Kusch, S., Frindte, K., Eckmeier, E., Jaeschke, A., Dunai, T., Fuentes, B., Mörchen, R., Schütte, T., Lücke, A., Klumpp, E., Kaiser, K., Rethemeyer, J., 2020. Tracing elevational changes in microbial life and organic carbon sources in soils of the Atacama Desert. Glob. Planet. Chang. 184, 103078.

Koch, M.A., Stock, C., Kleinpeter, D., Del Río, C., Osses, P., Merklinger, F.F., Quandt, D., Siegmund, A., 2020. Vegetation growth and landscape genetics of *Tillandsia* Lomas at their dry limits in the Atacama Desert show fine-scale response to environmental parameters. Ecol. Evol. 10, 13260–13274. https://doi.org/10.1002/ece3.6924.

Ladd, S.N., Maloney, A.E., Nelson, D.B., Prebble, M., Camperio, G., Sear, D.A., Hassall, J.D., Langdon, P.G., Sachs, J.P., Dubois, N., 2021. Leaf wax hydrogen isotopes as a hydroclimate proxy in the tropical Pacific. J. Geophys. Res. Biogeosci. 126 https://doi.org/10.1029/2020JG005891 e2020JG005891.

Latorre, C., Gonzáles, A.L., Quade, J., Farina, J.M., Pinto, R., Marquet, P.A., 2011. Establishment and formation of fog-dependent Tillandsia landbeckii dunes in the Atacama Desert: evidence from radiocarbon and stable isotopes. J. Geophys. Res. 116, G03033. https://doi.org/10.1029/2010JG001521.

Lester, E.D., Satomi, M., Ponce, A., 2007. Microflora of extreme arid Atacama Desert soils. Soil Biol. Biochem. 39, 704–708. https://doi.org/10.1016/j.soilbio.2006.09.020.

Lobos Roco, F., de Arellano, J.V.-G., Pedruzo-Bagazgoitia, X., 2018. Characterizing the influence of the marine stratocumu- lus cloud on the land fog at the Atacama Desert. Atmos. Res. 214, 109–120. https://doi.org/10.1016/j.atmosres.2018.07.009.

Lüning, S., Galka, M., Bamonte, F.P., Rodriguez, F.G., Vahrenholt, F., 2019. The medieval climate Anomaly in South America. Quat. Int. 508, 70–87. https://doi.org/10.1016/j.quaint.2018.10.041.

Lüttge, U., 2010. Ability of crassulacean acid metabolism plants to overcome interacting stresses in tropical environments. AoB Plants 2010. https://doi.org/10.1093/aobpla/plq005 plq005.

Mann, M.E., Zhang, Z., Rutherford, S., Bradley, R.S., Hughes, M.K., Shindell, D., Ammann, C., Faluvegi, G., Ni, F., 2009. Global signatures and dynamical origins of the little ice age and medieval climate anomaly. Science 326 (5957), 1256–1260.

Mantua, N.J., Hare, S.R., Zhang, Y., Wallace, J.M., Francis, R.C., 1997. A pacific Interdecadal climate oscillation with impacts on Salmon production. Bull. Am. Meteorol. Soc. 78, 1069–1079.

McMurdie, P.J., Holmes, S., 2013. phyloseq: an R package for reproducible interactive analysis and graphics of microbiome census data. PLoS One 8, e61217. https://doi.org/10.1371/journal.pone.0061217.

Mörchen, R., Lehndorff, E., Diaz, F.A., Moradi, G., Bol, R., Fuentes, B., Klumpp, E., Amelung, W., 2019. Carbon accrual in the Atacama Desert. Glob. Planet. Chang. 181, 102993 https://doi.org/10.1016/j.gloplacha.2019.102993.

Merklinger, F.F., Zheng, Y., Luebert, F., Harpke, D., Böhnert, T., Stoll, A., Koch, M.A., Blattner, F.R., Wiehe, T, Quandt, D., 2020. Population genomics of *Tillandsia landbeckii* reveals unbalanced genetic diversity and founder effects in the Atacama Desert. Glob. Planet. Chang. 184, 103076.

Mörchen, R., Amelung, W., Giese, C., Böhnert, T., Ruhm, J., Lehndorff, E., 2021. Fingerprint of plant life in the Atacama Desert – Insights from n-alkane analyses. Org. Geochem. 151 https://doi.org/10.1016/j.orggeochem.2020.104145.

Muñoz, R., Quintana, J., Falvey, M., Rutllant, J., Garreaud, R., 2016. Coastal clouds at the eastern margin of the Southeast Pacific: Climatology and trends. J. Clim. 29, 4525–4542. https://doi.org/10.1175/JCLI-D-15-0757.1.

Navarro-González, R., Rainey, F.A., Molina, P., Bagaley, D.R., Hollen, B.J., de La Rosa, J., Small, A.M., Quinn, R.C., Grunthaner, F.J., Caceres, L., Gomez-Silva, B., McKay, C.P., 2003. Mars-like soils in the Atacama Desert, Chile, and the dry limit of microbial life. Science 302, 1018–1021. https://doi.org/10.1126/science.1089143.

Neukom, R., Steiger, N., Gómez-Navarro, J.J., Wang, J., Werner, J.P., 2019. No evidence for globally coherent warm and cold periods over the preindustrial Common Era. Nature 571, 550–554. https://doi.org/10.1038/s41586-019-1401-2.

Ochsenreiter, T., Selezi, D., Quaiser, A., Bonch-Osmolovskaya, L., Schleper, C., 2003. Diversity and abundance of Crenarchaeota in terrestrial habitats studied by 16S RNA surveys and real time PCR. Environ. Microbiol. 5, 787–797.

Oksanen, J., Blanchet, F.G., Kindt, R., Legendre, P., Minchin, P.R., O'Hara, R.B., Solymos, P., Stevens, M.H.H., Szoecs, E., 2022. vegan: Community Ecology Package - R package version 2.6–2.

Olson, E.J., Dodd, J.P., Rivera, M.A., 2020. *Prosopis* sp. tree-ring oxygen and carbon isotope record of regional-scale hydroclimate variability during the last 9500 years in the Atacama Desert. Palaeogeogr. Palaeoclimatol. Palaeoecol. 538, 109408. https://doi.org/10.1016/j.palaeo.2019.109408.

Philben, M., Bowering, K., Podrebarac, F.A., Laganière, J., Edwards, K., Ziegler, S.E., 2022. Enrichment of ^{13}C with depth in soil organic horizons is not explained by CO_2 or DOC losses during decomposition. Geoderma 424, 116004. https://doi.org/10.1016/j.geoderma.2022.116004.

Pinkart, H., Ringelberg, D., Piceno, Y., Macnaughton, S., White, D.C., 2002. Biochemical approaches to biomass measurements and community structure analysis. In: Hurst, C.J. (Ed.), Manual of Environmental Microbiology, second ed. ASM Press, Washington, DC, pp. 101–113.

Pinto, R., Barria, I., Marquet, P.A., 2006. Geographical distribution of Tillandsia lomas in the Atacama Desert, northern Chile. J. Arid Environ. 65, 543–552. https://doi.org/10.1016/j.jarid env.2005.08.015.

Prieto, I., Almagro, M., Bastida, F., Querejeta, J.I., 2019. Altered leaf litter quality exacerbates the negative impact of climate change on decomposition. J. Ecol. 107, 2364–2384. https://doi.org/10.1111/1365-2745.13168.

Quade, J., Rech, J.A., Latorre, C., Betancourt, J., Gleeson, E., Kalin, M.T.K., 2007. Soils at the hyperarid margin: the isotopic composition of soil carbonate from the Atacama Desert, northern Chile. Geochim. Cosmochim. Acta 71, 3772–3795.

Quast, C., Pruesse, E., Yilmaz, P., Gerken, J., Schweer, T., Yarza, P., 2013. The SILVA ribosomal RNA gene database project: improved data processing and web-based tools. Nucleic Acids Res. 41 (D1). D590-D6.

Raux, P.S., Gravelle, S., Dumais, J., 2020. Design of a unidirectional water valve in Tillandsia. Nat. Commun. 11, 1–7. https://doi.org/10.1038/s41467-019-14,236-5.

Rethemeyer, J., Gierga, M., Heinze, S., Stolz, A., Wotte, A., Wischhöfer, P., Berg, S., Melchert, J.O., Dewald, A., 2019. Current sample preparation and analytical capabilities of the radiocarbon laboratory at CologneAMS. Radiocarbon 61 (5), 1449–1460. https://doi.org/10.1017/RDC.2019.16.

Ritter, B., Wennrich, V., Medialdea, A., Brill, D., King, G., Schneiderwind, S., Niemann, K., Fernandez-Galego, E., Diederich, J., Rolf, C., Bao, R., Melles, M., Dunai, T., 2019. Climatic fluctuations in the hyperarid core of the Atacama Desert during the past 215 ka. Sci. Rep. 9 (1), 5270.

Robinson, D., 2001. $\delta^{15}N$ as an integrator of the nitrogen cycle. Trends Ecol. Evol. 16, 153–162.

Rosinger, C., Rousk, J., Bonkowski, M., Rethemeyer, J., Jaeschke, A., 2023. Rewetting the hyper-arid Atacama Desert soil reactivates a carbon-starved microbial decomposer community and also triggers archaeal metabolism. Sci. Total Environ. 892 (164), 785. https://doi.org/10.1016/j.scitotenv.2023.164785.

Rundel, P.W., Dillon, M.O., 1998. Ecological patterns in the Bromeliaceae of the Lomas formations of Coastal Chile and Peru. Pl. Syst. Evol. 212, 261–278.

Rundel, P.W., Palma, B., Dillon, M.O., Sharifi, M.R., Nilsen, E.T., Boonpragob, K., 1997. Tillandsia landbeckii in the coastal Atacama Desert of northern Chile. Rev. Chil. Hist. Nat. 70, 341–349.

Sachse, D., Billault, I., Bowen, G.J., Chikaraishi, Y., Dawson, T.E., Feakins, S.E., Freeman, K.H., Magill, C.R., McInerney, F.A., Van der Meer, M.T.J., Polissar, P., Robins, R.J., Sachs, J.P., Schmidt, H.L., Sessions, A.L., White, J.W.C., West, J.B., Kahmen, A., 2012. Molecular paleohydrology: interpreting the hydrogen-isotopic composition of lipid biomarkers from photosynthesizing organisms. Annu. Rev. Earth Planet. Sci. 40, 221–249.

Sager, C., Airo, A., Mangelsdorf, K., Arens, F.L., Karger, C., Schulze-Makuch, D., 2023. Habitability of polygonal soils in the hyper-arid Atacama Desert after a simulated rain experiment. J. Geophys. Res.-Biogeosci. 128 https://doi.org/10.1029/2022JG007328 e2022JG007328.

Schefuß, E., Schouten, S., Schneider, R.R., 2005. Climatic controls on central African hydrology during the past 20,000 years. Nature 437, 1003–1006.

Schouten, S., Hopmans, E.C., Sinninghe Damsté, J.S., 2013. The organic geochemistry of glycerol dialkyl glycerol tetraether lipids: a review. Org. Geochem. 54, 19–61.

Schulz, N., Boisier, J.P., Aceituno, P., 2011. Climate change along the arid coast of northern Chile. J. Clim. 32, 1803–1814. https://doi.org/10.1002/joc.2395.

Schulze-Makuch, D., Wagner, D., Kounaves, S.P., Mangelsdorf, K., Devine, K.G., de Vera, J.-P., Schmitt-Kopplin, P., Grossart, H.-P., Parro, V., Kaupenjohann, M., Galy, A., Schneider, B., Airo, A., Frösler, J., Davila, A.F., Arens, F.L., Cáceres, L., Cornejo, F.S., Carrizo, D., Dartnell, L., DiRuggiero, J., Flury, M., Ganzert, L., Gessner, M.O., Grathwohl, P., Guan, L., Heinz, J., Hess, M., Keppler, F., Maus, D., McKay, C.P., Meckenstock, R.U., Montgomery, W., Oberlin, E.A., Probst, A.J., Sáenz, J.S., Sattler, T., Schirmack, J., Sephton, M.A., Schloter, M., Uhl, J., Valenzuela, B., Vestergaard, G., Wörmer, L., Zamorano, P., 2018. Transitory

microbial habitat in the hyperarid Atacama Desert. Proc. Natl. Acad. Sci. USA 115, 2670–2675. https://doi.org/10.1073/pnas.1714341115.

Schween, J.H., Hoffmeister, D., Loehnert, U., 2020. Filling the observational gap in the Atacama Desert with a new network of climate stations. Glob. Planet. Chang. 184 (103), 034. https://doi.org/10.1016/j.gloplacha.2019.103034.

Shen, J., 2020. Phospholipid biomarkers in Mars-analogous soils of the Atacama Desert. Int. J. Astrobiol. 19, 505–514.

Shen, J., Zerkle, A.L., Stueeken, E., Claire, M.W., 2019. Nitrates as a potential N supply for microbial ecosystems in a hyperarid Mars analog system. Life 9, 79.

Soderberg, K., 2010. The Role of Fog in the Ecohydrology and Biogeochemistry of the Namib Desert. PhD thesis,. University of Virginia, USA.

Sternberg, L., Deniro, M.J., Ajie, H., 1984. Stable hydrogen isotope ratios of saponifiable lipids and cellulose nitrate from CAM, C-3 and C-4 plants. Phytochemistry 23, 2475–2477.

Stuiver, M., Reimer, P., Reimer, R., 2020. CALIB 8.2. http://calib.org/calib/.

Takai, K., Horikoshi, K., 2000. Rapid detection and quantification of members of the archaeal community by quantitative PCR using fluorogenic probes. Appl. Environ. Microbiol. 66 (11), 5066–5072.

Trenberth, K.E., Fasullo, J.T., 2013. An apparent hiatus in global warming? Earth's Future 1, 19–32. https://doi.org/10.1002/2013EF000165.

Villanueva, R.A.M., Chen, Z.J., 2019. ggplot2: elegant graphics for data analysis, 2nd edition. Meas-Interdiscip. Res. 17 (3), 160–167.

Voigt, C., Klipsch, S., Herwartz, D., Chong, G., Staubwasser, M., 2020. The spatial distribution of soluble salts in the surface soil of the Atacama Desert and their relationship to hyperaridity. Glob. Planet. Chang. 184, 103077. https://doi.org/10.1016/j.gloplacha.2019.103077.

Wang, C., Wang, X., Liu, D., Wu, H., Lü, X., Fang, Y., Cheng, W., Luo, W., Jiang, P., Shi, J., Yin, H., Zhou, J., Han, X., Bai, E., 2014. Aridity threshold in controlling ecosystem nitrogen cycling in arid and semi-arid grasslands. Nat. Commun. 5, 4799. https://doi.org/10.1038/ncomms5799.

Wei, S., Cui, H., Zhang, Y., Su, X., Dong, H., Chen, F., 2019. Comparative evaluation of three archaeal primer pairs for exploring archaeal communities in deep-sea sediments and permafrost soils. Extremophiles 23 (6), 747–757.

Wennrich, V., Brill, D., Carballeira, R., Hoffmeister, D., Jaeschke, A., Kerber, F., Maldonado, A., Olivares, L., Opitz, S., Rethemeyer, J., Reyers, M., Ritter, B., Schween, J.H., Sevinç, F., Walber-Hellmann, K., Melles, M., 2023. Late Pleistocene to modern precipitation changes at the Paranal clay pan, central Atacama Desert. Glob. Planet. Chang. 233 (104), 349. https://doi.org/10.1016/j.gloplacha.2023.104349.

Wierzchos, J., Cámara, B., de Los Ríos, A., Davila, A.F., Sánchez Almazo, I.M., Artieda, O., Wierzchos, K., Gomez-Silva, B., McKay, C.P., Ascaso, C., 2011. Microbial colonization of Ca-sulfate crusts in the hyperarid core of the Atacama Desert: Implications for the search for life on Mars. Geobiology 9 (1), 44–60. https://doi.org/10.1111/j.1472-4669.2010.00254.x.

Wilhelm, M.B., Davila, A.F., Eigenbrode, J.L., Parenteau, M.N., Jahnke, L.L., Liu, X.L., Summons, R.E., Wray, J.J., Stamos, B.N., O'Reilly, S.S., Williams, A., 2017. Xeropreservation of functionalized lipid biomarkers in hyperarid soils in the Atacama Desert. Org. Geochem. 103, 97–104.

Willers, C., Jansen van Rensburg, P.J., Claassens, S., 2015. Phospholipid fatty acid profiling of microbial communities-a review of interpretations and recent applications. Appl. Microbiol. 119, 1207–1218. https://doi.org/10.1111/jam.12902.

Yilmaz, P., Parfrey, L.W., Yarza, P., Gerken, J., Pruesse, E., Quast, C., 2014. The SILVA and "All-species Living Tree Project (LTP)" taxonomic frameworks. Nucleic Acids Res. 42 (D1). D643-D8.